RUPTURE DYNAMICS OF STRIKE-SLIP FAULTS WITH STEPOVERS: FROM CONCEPTUALLY SIMPLIFIED TO REALISTICALLY COMPLEX FAULT SYSTEMS

A Dissertation

by

ZAIFENG LIU

Submitted to the Office of Graduate and Professional Studies of
Texas A&M University
in partial fulfillment of the requirements for the degree of

DOCTOR OF PHILOSOPHY

Chair of Committee,	Benchun Duan
Committee Members,	Frederic M. Chester
	Judith Chester
	Andreas Kronenberg
	Luciana R. Barroso
Head of Department,	Rick Giardino

May 2014

Major Subject: Geophysics

ABSTRACT

This dissertation investigates the interaction of model II in-plane dynamic rupture with a geometrical discontinuity along the fault strike: stepover. One goal is to understand how large the stepover width must be to stop the dynamic rupture, and whether the maximum width is affected by the undrained pore pressure and the off-fault damage during the coseismic process in conceptually simplified faults. In this research, we want to understand the rupture dynamics in a realistically complex stepover, the Aksay double-bend in the Altyn Tagh fault, and its ability to stop the dynamic rupture.

A detailed parameter-space study has been performed in the simplified model. From the single fault test, I find that the Positive Coulomb Stress (PCS) region at the end of the first fault controls the rupture initiation time and location on the second fault. The effects of off-fault plastic deformation and undrained pore pressure on the rupture dynamics within this simplified model have been discussed separately. The coupling effect of those two effects has also been studied.

The possible correlation between the slip gradient nearby the first fault end and the ability of the rupture to jump over the structure stepover in the strike-slip fault system has been verified by my elastic models. I find that the slip gradients calculated over the final 1 km of fault have a linear relationship with both the corresponding average stress drop in the fault system and the largest width of the step that could be jumped by the propagating rupture.

In the model with realistically complex fault geometry, I use the slip and rate weakening law and the multi-cycle earthquake simulation method. I find that there are

multiple rupturing scenarios that could occur within this complex fault geometry. My statistic analysis of the results of one-hundred-cycles' simulations indicates that the Aksay bend successfully prevents nearly 90% events from propagating through it, which suggests that the Aksay bend works effectively as a barrier for coseismic ruptures. Viscosity in my models characterizes the effects of off-fault deformation on the faulting process. The results show that larger off-fault deformation strengthens the Aksay bend's ability to stop a seismic rupture.

ACKNOWLEDGEMENTS

This dissertation would never be finished without the help of a huge support group of people. I am strongly grateful and thankful for all the members in the tectonophyscial research center and G&G department.

I want first to give my special thanks to my advisor: Professor Benchun Duan. Ben has been a fantastic advisor in the entire course of my Ph.D. study. He introduced me into the field of rupture dynamic simulation and guided me through all those challenging research topics. I could not forget the time we worked together to discuss the Fortran code and Matlab code line by line. And the joyful moments we shared when we finally found a solution to the problems in our researches after several months' work.

I express my gratitude to Professor Frederick M. Chester, and he is one of my committee members. I met him the second day after I came to the G&G department. He helped me set up the office and the key ready. He is the best teacher I have ever met. I learned a lot from his "fracture and faulting" course.

My gratitude also goes to Professor Judith Chester. She was the teacher of my first class in Texas A&M. Even though that class was canceled finally due to the shortage of registered students, I was still impressed by her enthusiasm in teaching.

I also want to extend my gratitude to Professor Andreas Kronenberg and Professor Luciana R. Barroso, who kindly accepted my invitation to be my committee members, and helped me on deepening my research topic.

Special thanks go to my friends and colleagues in department of Geology and Geophysics. Thanks to Dr. Caleb Holyoke, Charles Choens, and Johnason Fry, my office

iv

neighbors. Those casual talks we had helped me understand our research center, our department, our university and even the society of United States. Special thanks to Harold Johnson, one of the nicest guys I have ever met and my office neighbor too.

Finally, thanks to my wife and daughter for accompanying me during my study, thesis writing. Thanks to my parents for consistent support and encouragement.

TABLE OF CONTENTS

LIST OF FIGURES

x

LIST OF TABLES

1. INTRODUCTION

What stops the seismic rupture on a certain fault? This is a question that requires the effort of multiple generations of seismologists. Previous researchers have paved multiple ways for us to follow, which have the potential to address this question. Two main directions have been intensively researched in the past several decades: 1. the heterogeneous distribution of frictional parameters, or the effect of sudden change of lithology or any other petrophysical property variations at the fault tip; 2. the geometry discontinuities: stepover, bend or any other sudden strike discontinuity or direction changes. In this dissertation, I focus on researching the effect of geometrical discontinuity along fault strike on stopping the seismic rupture first under homogenous frictional parameters, simplified normal and shear stresses on fault, then under a fault system with a realistically complex geometry and heterogeneous initial stresses. Because the precise description of the heterogeneous distribution of the frictional coefficients and stresses on the fault surface is so hard to obtain, I choose to narrow the scope of this dissertation down to the variation of fault geometry in two dimensions and the resulting heterogeneity of stresses.

In section 2, I study the stepover's ability to stop seismic rupture within a fault system consisting of two parallel strike-slip faults. Compared with previous researches about this topic, we involve the plastic off-fault behavior into our model to test its effect on rupture's jumping ability. Furthermore, the poroplastic off-fault behavior has also been examined. Our results enrich the existing researches on the stepover topic.

1

In section 3, I study the relationship between the shape of final slip on the first fault and the seismic rupture's ability to jump the stepover onto the second fault in the model consisting of two parallel strike-slip faults. This study is inspired by the research carried out by Elliott et al. (2009). They measured the slip gradient near the fault tip on many faults by digitizing those published slip measurements on faults after many earthquakes, and then proposed a threshold of the slip gradient measured 1 km away from the fault tip. If the final slip gradient on the fault is larger than the threshold, the seismic rupture propagating on it has a high possibility to successfully jump stepover locating at the end of the fault. Our simulation results confirm the close relationship between the slip gradient near the fault tip and the seismic rupture's jumping ability on the fault. Furthermore, we specify the relationship is linear on a fault with a fixed length and a fixed stress drop on it.

In section 4, we move from the simplified fault geometry to the field-measured fault geometry. We attempt to study the behavior of the dynamic rupture on the Aksay double-bend of the Altyn Tagh Fault locating in Gansu province, China. Furthermore, we analyze the role that the Aksay double-bend has played in stopping or restraining the seismic ruptures. The largest differences of our study compared with previously similar researches are the field-measured fault geometry in our model and the usage of multi-cycle earthquake simulation method developed by Duan and Olgesby (2006). The field-measured fault geometry allows us to compare our results with the filed measurements, including slip-rate and paleoseismic observations. The multi-cycle earthquake simulator allows us to set the number of simulated earthquake cycles, which provide us the chance

to statistically analyze the Aksay double-bend's effectiveness in stopping or restraining the seismic ruptures. The collaboration between the modelers and field geologists is also the bright spot of this research.

2. DYNAMICS OF PARALLEL STRIKE-SLIP FAULTS WITH PORE FLUID

PRESSURE CHANGE AND OFF-FAULT DAMAGE[*]

2.1 Introduction

In field observations, the traces of active faults where recent earthquake events could be observed are often discontinuous, and may consist of several segments which are separated by steps (Wesnousky, 1988). This geometrical feature has been proposed to control the final length of fault rupture (Sibson, 1985, 1986; Reasenberg et al., 1982), and to explain the location of basins (Burchfiel and Stewart, 1966). More quantitative studies have included the dislocation theory to quantitatively study the formation of basins in strike-slip systems, such as Rodgers (1980). However, Rodgers' analysis did not involve jumping rupture across a stepover. Segall and Pollard (1980) carried out a quasi-static analysis of earthquake rupture behavior at a stepover within a strike-slip fault system. Dynamic simulations of rupture propagation within a fault system with two parallel strike-slip faults embedded in an elastic medium were first performed by Harris et al. (1991) and detailed analyses were reported in Harris and Day (1993). Their numerical results about the maximum jumpable step width are consistent with Wesnousky's (1988) field observations. After summarizing 22 historical strike-slip earthquakes with rupture length from 10 to 420 km, Wesnousky (2006) found that roughly two-thirds of the measured steps acted as endpoints of strike-slip earthquake ruptures and those steps had widths larger than 3-4 km. On the other hand, when the step

width was smaller than 3-4 km, 60 percent of surveyed ruptures were able to propagate across the step.

Field surveys of large-scale strike-slip faults have revealed the existence of a fracture zone around main slip surfaces (e.g., Chester et al., 1993). To simulate this type of energy absorption effect, Andrews (2005) employed a nonelastic model with a Coulomb yielding criterion in the medium off the main slip surface to simulate dynamic rupture with energy loss outside the slip zone. He found that off-fault yielding affects rupture velocity and peak slip velocity. Off fault plasticity has been investigated intensively in recent years. Ben-Zion and Shi (2005) revealed that off-fault plasticity could stabilize slip velocity of a propagating rupture. Duan (2008a) examined effects of low-velocity fault zones on rupture dynamics and near-field ground motion when off-fault materials yield. The distribution of off-fault deformation along a bimaterial interface and the effect of inelastic deformation on rupture propagation along a strike-slip fault with a kink were investigated by Duan (2008b) and Duan and Day (2008), respectively. Templeton et al. (2008) and Viesca et al. (2008) examined factors that influence plastic deformation distribution in "dry" and undrained systems, respectively, including the angle between the fault trace and the maximum compressive stress, the seismic S ratio, and the closeness of initial stress in off-fault material to Mohr-Coulomb failure. Ma and Andrews (2010) discussed inelastic off-fault response in a three-dimensional strike-slip fault and point out that the off-fault plasticity is narrowly confined to the fault in depth and the distribution pattern is correlated with the cohesion of off-fault material: low cohesion (~5 MPa) material allows the inelastic zone broadens near the surface; while,

high cohesion (~10 MPa) material confines the inelastic deformation mostly at deeper depth. Finzi, Y. and S. Langer (2012) addressed the effect of lower rigidity within the stepover could significantly promote the rupture propagation through the stepover. Xu and Ben-Zion (2013) analyzed the spatial and temporal evolutions of non-local properties of the stress field and provided a quantitative description on the characteristics of the off-fault yielding at different scales.

Off-fault damage alters the dynamics stress field around a stepover, and thus is expected to affect the dynamics of earthquake ruptures on parallel strike-slip faults. This topic has not been systematically investigated before. In addition, detailed quantitative analyses of the effects of time-dependent pore pressure (undrained systems) on dynamic rupture propagation across stepovers have not been performed in great detail, although Harris and Day (1993) presented an investigation into this topic for the case of elastic off-fault deformation. This paper is intended to improve our understanding of the effects of off-fault damage in the form of plastic yielding, and time-dependent pore- pressure changes (undrained systems), both of which likely operate during large strike-slip earthquakes.

2.2 Method

We use the finite-element code EQdyna (Duan and Oglesby, 2006; Duan and Day, 2008) to perform the dynamic earthquake rupture simulations in this study. The code is verified in a community-wide effort (Harris et al, 2009; 2011).

2.2.1 Model setup

We work with 2D strike-slip faulting models, similar to those analyzed by Harris and Day (1993). In Figure 2.1, two left lateral strike-slip fault segments with half length 14 km are embedded in a homogeneous medium. We primarily examine the case with the angle between maximum principle stress and the fault surfaces being 45^0. In this case, three stress components, $\sigma_{11} = \sigma_{22}$ and σ_{21}, define the initial stress field, which is homogenous and is assigned in the entire medium. The initial stress field, fault slip sense and length are similar to those used by Harris and Day (1993). We choose the static coefficient of friction to be 0.75 (Byerlee,1978), and the dynamic coefficient of friction to be 0.3. The length of the fault segments' overlap has been adjusted to make sure the overlap would not affect the jumping ability and 3 km is the value we select. We examine stepover widths in increments of 500 meters on both the dilatational and compressive sides of the first fault. Furthermore, Harris and Day (1993) also discuss rupture's jumping ability in both the supershear ($S = \frac{\tau_p - \sigma_{21}}{\sigma_{21} - \tau_r} < 1.63$) and subshear ($S = \frac{\tau_p - \sigma_{21}}{\sigma_{21} - \tau_r} > 1.63$) ruptures in elastic models, where $\tau_p = f_s(-\sigma_n)$ and $\tau_r = f_d(-\sigma_n)$ are the static and dynamic friction, respectively, and the compressive normal stress is a negative value. We will only focus on the supershear rupture case, because the subshear rupture would have very limited ability to jump stepovers.

The rupture is initiated at the middle of the first fault (the nucleation point), and is forced to grow outward at a certain speed within a nucleation patch Lc (Day, 1982; Andrews, 1976, 1985). Outside the nucleation patch, rupture propagates spontaneously

on the first fault. We examine whether and how the rupture may propagate across a

stepover onto the second fault.
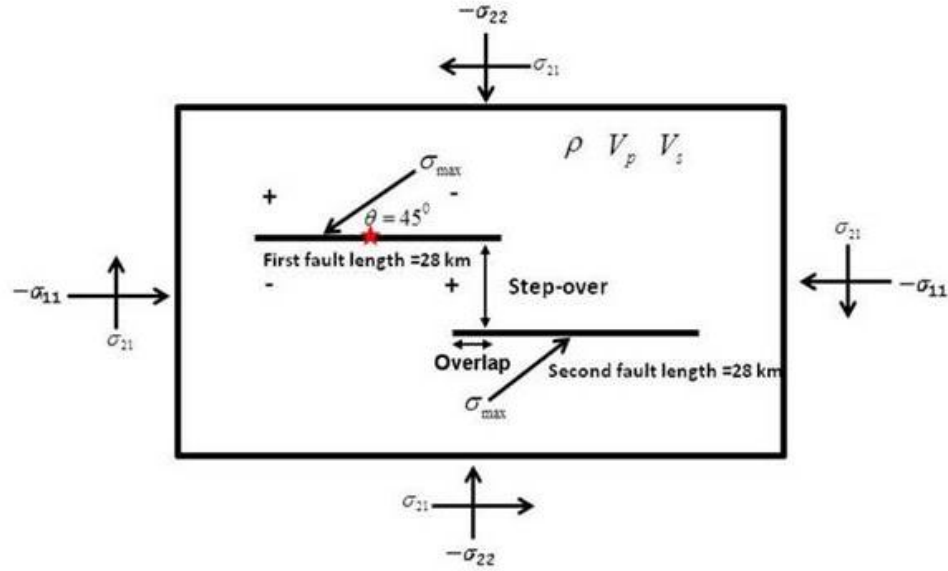
Figure 2. 1 The model geometry, sense of slip and initial stress in our calculations. Two parallel left-lateral strike-slip faults are imbedded in a homogeneous elastic or elastoplastic medium. Compressional and dilatational quadrants around the first fault are labeled by plus (+) and minus (-) signs, respectively. The convention of compressive normal stress is negative has been employed.

2.2.2 Fault frictional behavior

We regard the earthquake rupture as a frictional behavior on a pre-existing fault surface. The evolution of frictional coefficient is approximated by a slip-weakening law (Ida, 1972; Palmer and Rice, 1973) in which the static friction decreases to the dynamic friction value after a critical slip distance $D_0 = 0.5$ m on the fault.

$$f = \begin{cases} f_s - \dfrac{(f_s - f_d)\Delta u}{D_0} \;, & \Delta u \leq D_0 \\ f_d \;, & \Delta u > D_0 \end{cases} \tag{2.1}$$

where f_s and f_d are the static and dynamic coefficients of friction, respectively.

2.2.3 Off-fault elastoplastic behavior

We know that rock yield beyond the elastic limit. The onset of inelastic deformation depends on the effective mean normal stress, i.e., $\sigma_m = \dfrac{\sigma'_{11}+\sigma'_{22}}{2}$ in two dimensions, for rocks. σ'_{11} and σ'_{22} are the effective normal stresses under the constant pore pressure: 20 MPa. Inelastic deformation may present itself in the form of frictional sliding on existing micro-fractures or micro-cracking. A Mohr-Coulomb yield criterion is used to characterize the inelastic behavior in the off-fault medium. In two dimensions, the maximum shear stress is:

$$= \sqrt{\frac{2}{21} + (\frac{(\sigma_{11} - \sigma'_{22})}{2})^2} \tag{2.2}$$

For an internal coefficient of friction $\tan \emptyset$ and cohesion c, the Coulomb criterion is:

$$\leq c\cos\emptyset - \left(\frac{1}{2}\right)(\sigma_{11} + \sigma_{22})\sin\emptyset \tag{2.3}$$

The negative sign on the right side of the equation corresponds to the convention that stress is positive. We remark that the Mohr-Coulomb yielding is just an idealization and approximation of rock behavior after reaching the yield point. If off-fault material violates the Mohr-Coulomb criterion, three stress components would be adjusted in the stress deviator domain (Andrews, 2005). A parameter CF (Closeness to Failure) can be defined with respect to the initial effective normal stresses and initial shear stress according to the equation in Figure 2.2.
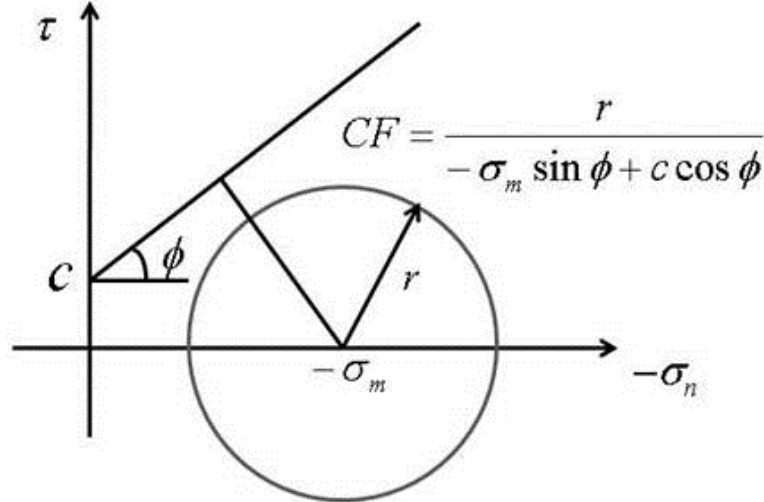
Figure 2. 2 Mohr-Coulomb yield criteria for off-fault plastic deformation. c is the cohesion and $\emptyset$ is the internal friction angle, and the closeness of stress state to failure is defined by CF.

2.2.4 Undrained pore pressure effect in the elastic case

Pore pressure change during rupture propagation in the elastic case has been discussed previously by Sibson (1985, 1986), Rice and Cleary (1976), and Harris and Day (1993). Sibson (1985) proposed that the reduced normal and mean stress at a dilatational stepover would suddenly open extension fractures. The fluid pressure in the extension fractures would not have enough time to re-equilibrate during the time of the earthquake, and then the effective normal stress would suddenly increase, resulting in an increase in the frictional strength at the dilatational stepover. The pore pressure change is determined by the following equation:

$$\Delta P(t) = -B \times \Delta\sigma_{kk}(t)\big/3 \qquad (2.4)$$

according to Rice and Cleary (1976). B is the Skempton's coefficient, and $\Delta\sigma_{kk}(t)\big/3$ is the time-dependent change in the total mean stress. For plane strain model, the strain is zero in the third direction:

$$\Delta P(t) = -B \left[(1 + v_u)\big/3 \right] (\Delta\sigma_{11}(t) + \Delta\sigma_{22}(t)) \qquad (2.5)$$

where v_u is the undrained Poisson ratio (Rice and Cleary, 1976).

2.2.5 Off-fault poroelastoplastic behavior

Viesca et al. (2008) point out the poroelastoplastic behavior could be simply using elastoplastic behavior with altered plasticity parameters, and the corresponding altered

11

plastic parameters could be calculated by proposed equations. Drucker-Prager yield criterion has been used in their research: $\tilde{\tau} + \mu \frac{\sigma_{kk}}{3} = b$, here b is the cohesion, μ is the internal friction, $\tilde{\tau} = \sqrt{(\frac{1}{2})s_{ij}s_{ij}}$, the second invariant of the deviatoric stress $s_{ij} = \sigma_{ij} - \delta_{ij}{}^{\sigma_{kk}}/_3$. In plane strain, the Drucker-Prager (DP) yield criterion approximates the Mohr-Coulomb (MC) (Templeton and Rice, 2008), which takes the form: $\max (\tau + (tan\emptyset)\sigma_n) = c$, where τ and σ_n are the shear and normal traction on any plane, $tan\emptyset$ is the internal friction coefficient and c is the cohesion. The DP and MC criteria coincide exactly for 2-D stress states when the out of plane principle stress is given by $\sigma_{33} = (\sigma_{11} + \sigma_{22})/_2 = {}^{\sigma_{kk}}/_3$. For those stress states, the cohesion and friction coefficients are related by $b = c\ cos\emptyset$ and $\mu = sin\emptyset$.

We use the equations proposed by Viesca et al. (2008) in the Drucker-Prager yield criterion to derive poroelastoplastic equations in the Mohr-Coulomb criterion. Viesca et al. (2008) propose that the undrained elastoplastic mechanism could be transformed into the drained elastoplastic mechanism with modified material parameters. This means an undrained elastoplastic model is interchangeable to a drained elastoplastic model (without influence from undrained pore pressure) mathematically with changes in material parameters. Viesca et al. (2008) propose the corresponding undrained DP criterion is: $\tilde{\tau} + \mu_u \frac{\sigma_{kk}}{3} = b_u$; $\mu_u = (1 - B)\mu = (1 - B)sin\emptyset$; $b_u = b - B\mu\sigma_m^0$, in a three-dimensional model. In a two-dimensional model, we employ the equation: $b_u = b - \frac{(1+v_u)}{3}B\mu\sigma_m^0 = c * cos\emptyset - \frac{1+v_u}{3}B\sigma_m^0 sin\emptyset$ and $\mu_u = (1 - B)\mu$ (Ma, 2012).

Now, we could derive the mathematically equivalent undrained MC criterion: $\tau + (tan\emptyset_u)\sigma_n = c_u$; in which

$$\emptyset_u = \arcsin\left((1-B)sin\emptyset\right) \tag{2.6}$$

$$C_u = \frac{Ccos\emptyset - (\frac{1+v_u}{3})Bsin\emptyset\sigma_m^0}{\cos\left(\arcsin\left((1-B)sin\emptyset\right)\right)} \tag{2.7}$$

B is the Skempton's coefficient and σ_m^0 is the original mean stress, which equals $\frac{\sigma_{11}+\sigma_{22}}{2}$. We just need to replace the parameters in the elastoplastic model with the undrained parameters to simulate the poroelastoplastic off-fault behavior.

2.3 Results

We first calculate a reference case of a dynamically propagating rupture on parallel strike-slip faults with off-fault elastic behavior and constant pore pressure, and in this case we neglect any dynamic pore pressure variation during rupture propagation, which is similar to the "dry" materials in both researches by Harris and Day (1993) and Templeton and Rice (2008). Then we separately explore the effects of time-dependent pore pressure (i.e., an undrained system) and off-fault damage. Finally, we examine the combined effects of the two factors. We report jumping positions on the parallel second fault and the time needed for rupture to jump in each case in the two parallel faults model.

To understand jumping positions and the maximum jumpable stepover width, we also perform the single fault test (i.e., just the first fault exists in the model) and calculate the Coulomb stress evolution on the parallel receiver fault. The Coulomb stress is

13

defined as $|\sigma_\tau| - \mu_s|\sigma_n|$, where σ_τ and σ_n are the shear stress and effective normal stress resolved on the parallel receiver fault, and μ_s is the static friction coefficient. We particularly examine the distribution of positive Coulomb stress (PCS) in the single fault test and its control on rupture jumping behavior across stepovers, by comparing the PCS history with the jumping time and position results in the two parallel faults model. Harris and Day (1993) point out that the single fault study can only check if the resolved shear stress is larger than the static friction on the receiver fault (the second fault), so the possible jumping position on second fault could be determined, but it is insufficient to evaluate if the stress concentration is enough to successfully induce rupture propagation on the

Receiver fault (the second fault). Therefore, in our simulation, we only check if the rupture could or could not successfully initiate on the second fault, and ignore the ability of the rupture to sustain itself on the second fault. We perform simulations of both single-fault and two-fault models in each case.

2.3.1 Elastic case with negligible changes in pore pressure (the elastic case)

In this section, we present the results from one set of elastic calculations whose parameters are listed in Table 2.1. In this case, the presetting pore pressure (20.0 MPa) is incorporated in the initial stresses, but it has negligible changes during the dynamic rupture propagation. For each set, we run 20 or more simulations with a termination time of 15 seconds for different widths of the stepover with an interval of 500 meters. We do not set any constraint on the maximum stepover width that could be jumped. In the

elastic case, the rupture takes 3.479 s to reach the end of the first fault. The rupture is triggered at different times on the second fault. The maximum jumpable widths in the dilatational and compressive stepovers are 5000 m and 3500 m, respectively. Figure 2.3(a) summarizes the location of rupture being triggered on the second fault, and Figure 2.4(a) shows the time interval between the time rupture arrives at the end of the first fault and the time rupture is triggered on the second fault in this case. We observed that the rupture needs more time to be initiated on the second fault in the dilatational stepover than in the compressive stepovers. Moreover, in dilatational steps, the initiation position on the second fault is within the stepover and migrates towards the center of the first fault with an increase of the stepover width. On the other hand, in compressive stepovers, the initiation position on the second fault is beyond the stepover and gradually moves away from the stepover with increase of the stepover width. These observations are consistent with those reported by Harris and Day (1993).

Table 2.1 Material and computational parameters in model of elasticity

Parameter	Value
Density	2700 kg/m^3
Vp	6000 m/s
Vs	3464 m/s
Initial normal stress: σ_{11}, σ_{22}	-53.3 MPa
Initial shear stress: σ_{21}	20.0 MPa
Initial pore pressure	20.0 MPa
Static coefficient of friction	0.75
Dynamic coefficient of friction	0.30

Figure 2.3 Summary (map view) of the results of simulations of faults steps in left-lateral shear in our calculations. Positive width represents dilatational stepover and negative width represents compressional stepover. (a) Elastic case with drianed pore pressure. (b) Elastic case with undrained pore pressure. (c) Elastoplastic case with drained pore pressure. (d) Elastoplastic case with undrained pore pressure. The line in each case represents part of the first fault nearing the overlap, dots represent the triggered position of rupture on the second fault and the times to the right of the figure are the time of triggered ruptures on the second fault.

17

Figure 2.4 Summary of time needed for rupture to jump stepover from the first fault to the second fault. (a), (b), (c), (d) have the same meanings as in Figure 2.3.

In order to have a better understanding of the jumping ability of rupture, we use the single-fault test results to examine the Coulomb stress variation around fault one during the dynamic rupture process. In the single-fault test, we just remove the second fault and keep the first fault intact in the model configuration. Figure 2.5 shows the stress distribution around the first fault at 7s, which is roughly 3.5 s after the rupture reaching the first fault end. As expected, the shear stress component is symmetrical about the fault; while the effective normal stress component at the end varies dramatically. In the dilatational quadrant, there is a relative high stress lobe followed by a low stress lobe. We further examine the Coulomb stress distribution at this time, and find that the region of the positive Coulomb stress is precisely consistent with the distribution of the rupture initiation position on the second fault (Figure 2.3(a)). Therefore, the initiation position of rupture on the second fault is controlled by the spatial distribution of the positive Coulomb stress (PCS).

Because off-fault shear stress is symmetric about the fault in both quadrants, it is the effective normal stress that determines the different distribution of the PCS stress in the two quadrants of the first fault. We plot the effective normal stress distribution after the rupture reaches the fault end (Figure 2.6(a)), and find that there is a high effective normal stress patch in the dilatational quadrant and a low effective normal stress patch in the compressive quadrant propagating away from the first fault end. Therefore, the PCS in the compressive quadrant is generated by the low effective normal stress patch, and it is associated with the P wave propagation.

19

The PCS history in Figure 2.7(a) more clearly illustrates how the PCS controls the location and time of initiation of rupture on the second fault. At 4.0 seconds, the rupture just reaches the first fault end. The PCS has a larger extent in the compressive quadrant than in the dilatational quadrant. This explains why at the width of 1500 meters, rupture initiates on the second fault earlier in the compressive stepover than in the dilatational stepover (Figures 2.3(a) and 2.4(a)). At 4.5 seconds, there is a crescent-shaped PCS patch leaving the fault end and propagating towards the southeast direction into the compressive quadrant of the fault one. From 4.5 to 6.0 seconds, this PCS patch would initiate rupture on the second fault over the region it sweeps. We remark that the strength (i.e., the maximum PCS value) of this patch decreases as it propagates away from the first fault and it dies out after about 6.0 seconds. The lobe shape positive Coulomb stress region around the first fault end keeps expanding in both quadrants of the first fault. This lobe and its expanding control the time and position of initiation of rupture on the second fault in a dilatational stepover.
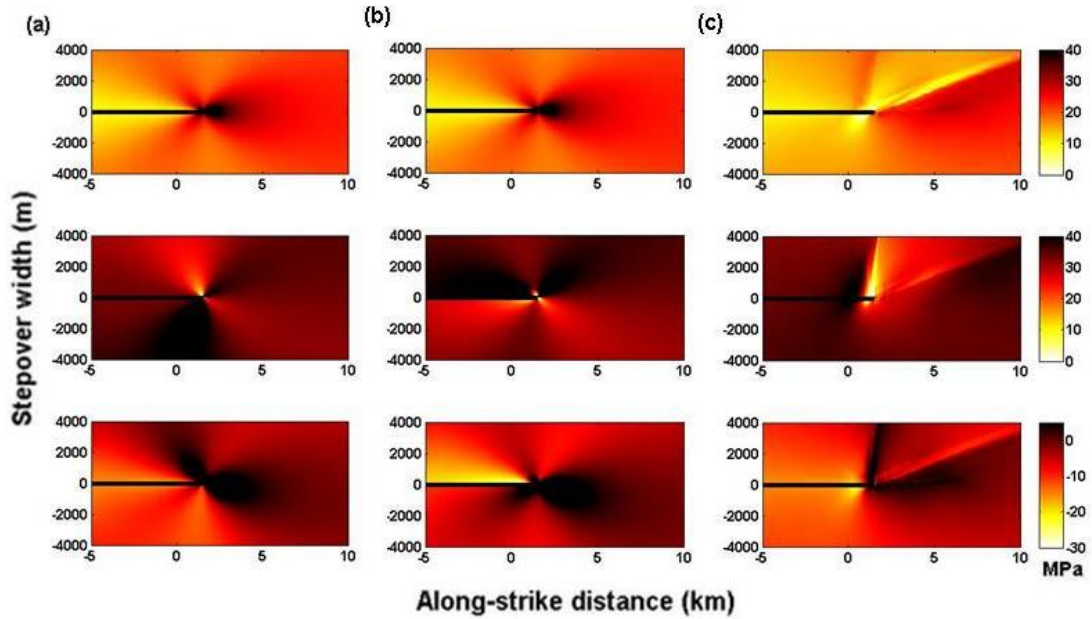
Figure 2.5 Summary of results from single fault test: fault shear (top panels), absolute value of fault normal (middle panels) stresses and Coulomb stress (bottom panels) around the first fault in one fault test after the propagating rupture arrives at the fault end in (a) the elastic case with drained pore pressure, (b) the elastic case with undrained pore pressure, and (c) the elastoplastic case with drained pore pressure.
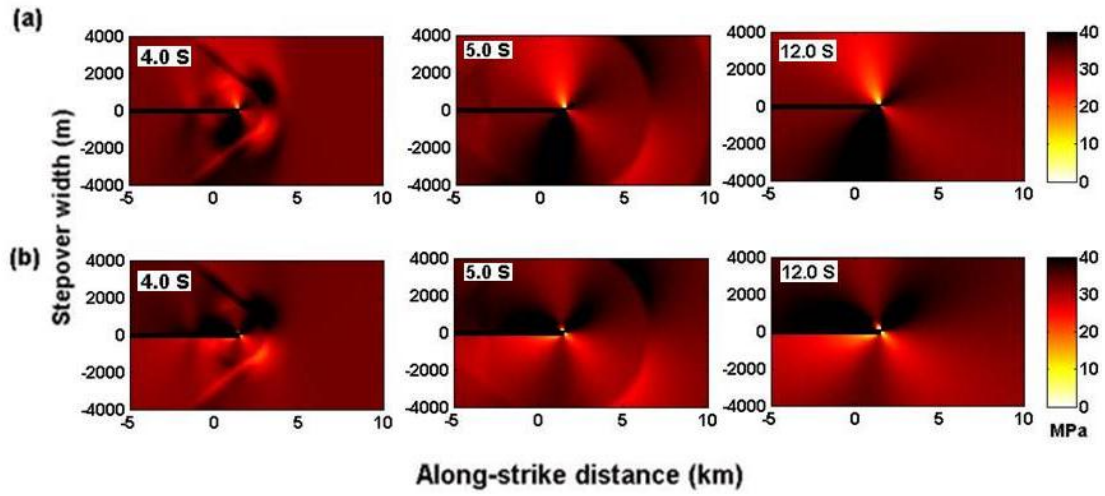
Figure 2.6 The time-dependent history of the absolute value of effective normal stress in the fault-normal direction in (a) elastic case with drained pore pressure and (b) elastic case with undrained pore pressure in the single fault test.
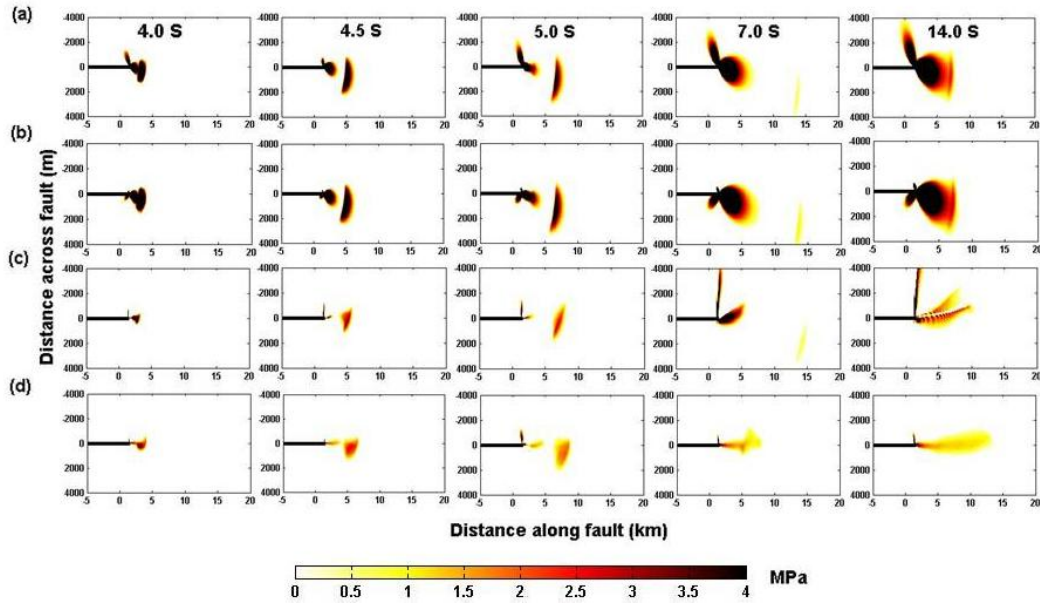
Figure 2.7 The history of the Positive Coulomb Stress (PCS) in single fault test. (a) the elastic case with drained pore pressure. (b) the elastic case with undrained pore pressure. (c) the elastoplastic case with drained pore pressure. (d) the elastoplastic case with undrained pore pressure.

2.3.2 Elastic case with undrained pore pressure (the poroelastic case)

The effect of undrained pore pressure in parallel strike-slip fault systems has been discussed preliminarily by Harris and Day (1993). They reported that the maximum dilatational stepover width jumpable to propagating earthquake rupture is greatly reduced by the existence of pore pressure change. In this section, we perform a detailed

quantitative analysis of its effect, and we set the undrained Poisson ratio to be 0.25 and the Skempton's coefficient to be 0.8.

Figures 2.3(b) and 2.4(b) show the locations of rupture being triggered on the second fault and the corresponding time needed to jump over varying stepovers, respectively. As reported by Harris and Day (1993), the maximum jumpable width of the dilatational stepover is reduced significantly by the influence of time-dependent pore pressure: from 5000 meters in the negligible pore pressure case to 1000 meters in this case. The time needed for the rupture to jump over the same stepover also increases significantly, e.g., from 0.386 s in the constant pore pressure case to 5.038 s for the 1000 meters wide dilatational stepover. At the compressive stepover, the maximum jumpable width increases from 3500 m to 4500 m.

Figure 2.6(b) shows the snapshot of the effective fault normal stress in the off-fault medium. At 4.0 seconds, the nearby effective normal stress is dominated by a high value lobe in the dilatational quadrant. While in the compressive quadrant, a low effective normal stress lobe occupies the nearby off-fault region, and the lobe is larger than the case of constant pore pressure. This distribution has been intensified around the fault end in subsequent calculation times.

Figure 2.7(b) shows the snapshot of the PCS in this case. Comparing with constant pore pressure (Figure 2.7(a)), time-dependent pore pressure imposes significant effects on the PCS distribution in the dilatational quadrant. The PCS lobe extending into the dilatational quadrant at an oblique (but high) angle with the fault in the constant pore pressure case (Figure 2.7(a)) cannot be developed in this case due to pore pressure

24

changes (Figure 2.7(b)). This results in significant reduction in the stepover width that can be jumped by a propagating rupture across the dilatational stepover. In this case, the PCS lobe that grows beyond the fault end is responsible for the rupture being able to propagate through 500 m and 1000m wide dilatational stepovers. It takes more than 5 seconds (after the rupture reaches the fault end) for the lobe to grow about 1000 m into the dilatational stepover, triggering rupture on the second fault rupture (Figure 2.4(b)). It cannot grow farther in the dilatational stepover due to reduced pore pressure and thus increased effective normal stress, resulting in the maximum jumpable width of about 1000 m in this model. Time-dependent pore pressure also affects the PCS distribution in the compressive quadrant. A small PCS lobe extending from the fault end, which is absent in the reference case (Figure 2.7(a)), grows with time due to time-dependent pore pressure. The PCS lobe that grows beyond the fault end has a larger extent and amplitude due to increased pore pressure and thus reduced effective normal stress in the compressive stepover. A close comparison between Figure 2.7(a) and 2.7(b) at 5.0 seconds indicates the split crescent-shaped PCS patch extends further into the compressive quadrant in the case of time-dependent pore pressure, which results in wider jumpable widths.

2.3.3. Case with inelastic off-fault deformation under negligible changes in pore pressure (the elastoplastic case)

In this section, we examine effects of off-fault damage in the form of plastic yielding on rupture dynamics of strike-slip faults with a stepover, assuming constant pore

pressure. To better illustrate possible effects, we present a set of models in which extensive plastic yielding occurs in dilatational quadrants of the first fault. In this set of models, internal frictional coefficient $(\tan \emptyset)$ and cohesion are 0.75 and 14.45, respectively, leading the value of closeness of failure (CF) to be 0.633.

Figure 2.3(c) summarizes the initiation position of triggered rupture on the second fault, and Figure 2.4(c) shows the time needed for rupture to jump in this case in the two parallel faults model. Compared with the elastic case with constant pore pressure, the obvious difference can be observed in the dilatational stepover. First, the rupture initiation position on the second fault occurs at the end of the first fault and does not migrate toward the center of the first fault. Second, the needed time is shorter than that in the elastic case, and the time difference in the two cases is proportional to the stepover width. On the other hand, effects for the compressive stepover are minor.

The aforementioned difference between the elastic case and the elastoplastic case in rupture behavior is caused by the stress distribution in dilatational stepovers, especially after the rupture arrives at the fault end, due to the occurrence of off-fault plastic deformation. In Figure 2.8, we show snapshots of off-fault plastic strain in the single-fault test after the rupture reaches the fault end. At 4 s, the off-fault plastic strain only occurs in the dilatational quadrant, and its width normal to the fault strike is proportional to the propagation distance, as reported by Andrews (2005). In the following several seconds, the re-equilibration of the stress field due to rupture deceleration and termination causes accumulation of plastic strain around the fault end. A strong plastic strain band makes an angle of $\sim 45^{\circ}$ with respect to the fault, and another band is roughly

26

perpendicular to the fault. Xu and Ben-Zoin (2013) attributed this increasing plastic

yielding zone to the increasing stress intensity factor associated with the decreasing

rupture speed at the fault end.
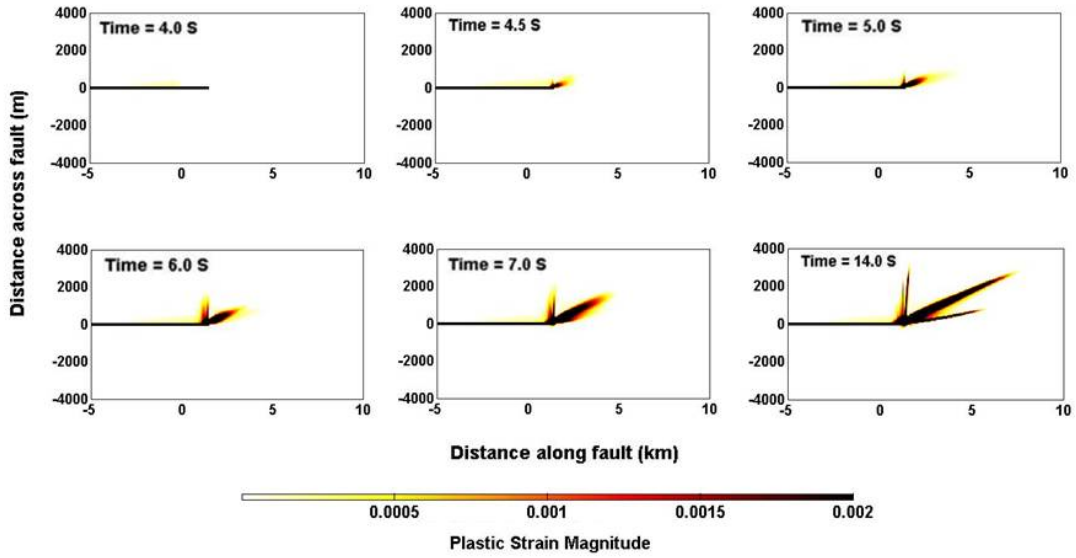
Figure 2.8 Snapshots of plastic strain distribution in elastoplastic case with constant pore pressure and CF=0.633 in the single fault test.

In Figure 2.7(c), we plot the PCS distribution history in the single fault test. A

triangular-shaped PCS patch, originating from the fault end and propagating into the

compressive quadrant, is similar to the crescent-shaped PCS patch in the elastic case

with constant pressure and would initiate rupture on a second parallel fault in the

compressive quadrant. However, the PCS distribution at the fault end is altered

significantly by off-fault plastic yielding. In the dilatational quadrant, a relatively narrow

PCS band grows roughly perpendicular to the fault strike with time. This PCS band controls the rupture time and position on the second fault in the dilatational stepover (Figure 2.3(c) and 2.4(c)). This PCS band appears to correlate with a strong plastic strain band that is nearly perpendicular to the fault strike (Figure 2.8), suggesting stress adjustment by off-fault damage in this band facilitates rupture to jump over a dilatational stepover onto a second parallel fault. Another PCS lobe extends from the fault end and grows in a direction close to the fault strike.

2.3.4 Case with inelastic off-fault deformation under an undrained pore pressure system

(the poroelastoplastic case)

Earthquake rupture may propagate under the influence of pore pressure changes and off-fault inelastic deformation, and even other factors, such as plastic hardening or weakening due to different rates of off-fault inelastic deformation or a low velocity fault zone. In this section, we examine the combined effects of time-dependent pore pressure and off-fault inelastic deformation with the same CF as the case under the constant pore pressure. By employing equations (2.6) and (2.7), we use internal friction coefficient $tan\emptyset = 0.12$ and cohesion $= 18.35$ as the undrained case, which corresponds to the elastoplastic case with the negligible pore pressure above and the corresponding CF=0.901.

Figure 2.3(d) and 2.4(d) summarize the initiation position of triggered rupture on the second fault and the time needed for the rupture to jump across the stepover in the two parallel faults model, respectively. Compared with the previous cases with only

28

undrained pore pressure or off-fault inelastic deformation, we find that the undrained pore pressure imposes the dominant effect on the jumping behavior of the propagating rupture, especially for a dilatational stepover. The jumpable width is much smaller (only 1500 m) for a dilatational stepover due to the effect of varying pore pressure, while in the compressive stepover, the jumpable width decreased by 500 m, compared with the elastoplastic case with constant pore pressure. The PCS time history in Figure 2.7(d) could help to explain the difference. The region of PCS in the dilatational quadrant has been strongly limited by the effect of undrained pore pressure. In the compressive quadrant, PCS has a larger extent in Figure 2.7(d) than that in Figure 2.7(c), which explains the increased 500 meters jumpable width in the compressive stepover. We believe that the plastic deformation occurring at the compressive quadrant (Figure 2.9) under the influence of varying pore pressure causes the change in the PCS distribution. Plastic deformation in the dilatational quadrant is also significantly limited in the extent by the varying pore pressure compared with the case of constant pore pressure.

Compared with the poroelastic case, the general pattern of rupture behavior has been kept. However, the initiation position of rupture on the second fault in the compressive quadrant moves farther away from the stepover along the strike direction compared with that in the poroelastic case. This may be explained by differences in the PCS distribution between the two cases (Figure 2.7(d) and 2.7(b)). In the compressive quadrant, the split crescent PCS, which controls the jumping location and time on the second fault, has a shorter extent in the direction perpendicular to the fault in figure 2.7(d) than that in figure 2.7(b) (e.g., 4.5 s and 5.0 s panels). Thus, the split crescent PCS sweeps the

second fault segment of the same stepover width at a distance farther away and at a later time in this case than that in the poroelastic case. On the other hand, the jumping position is mainly controlled by the PCS lobe extending from the fault end in the dilatational stepover, which appears extending to a farther distance in this case than that in the poroelastic case. Therefore, although pore pressure changes dominate in this case, off-fault damage still imposes some effects on the details of rupture initiation on the second fault.
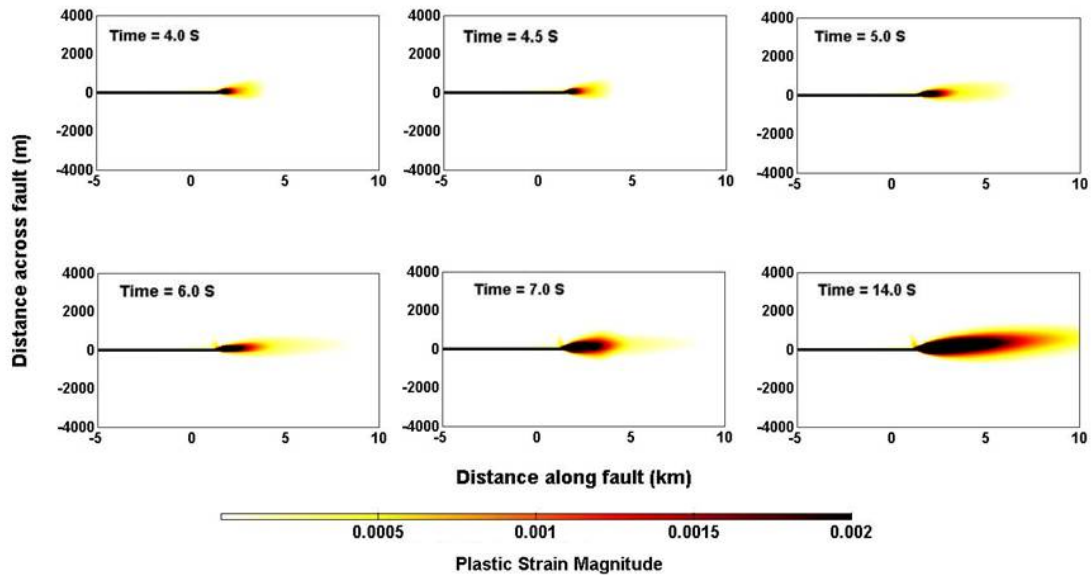
Figure 2.9   History of plastic strain distribution in elastoplastic case with undrained pore pressure and CF=0.901

2.4 Discussion

In this study, we mainly extend previous theoretical studies on rupture dynamics of parallel strike-slip faults (Harris et al., 1991; Harris and Day, 1993) from an elastic off-fault medium to an elastoplastic medium, and conduct a quantitative analysis of effects of pore pressure changes on rupture jumping behavior across a stepover. In the reference case (an elastic medium with constant pore pressure), our results of rupture jumping position and time across a stepover are consistent with those reported in the previous studies. Furthermore, we find that the distribution of the positive Coulomb stress using a single fault model is a powerful tool for gaining insights into rupture behavior across a stepover. In particular, we find that the time and position of rupture initiation on the second fault in the compressive stepover are controlled by a split crescent-shaped PCS patch that propagates away from the end of the first fault into the stepover, while they are controlled in the dilatational stepover by a PCS lobe that originates at the fault end and expands at a high angle with respect to the fault into the stepover.

In the case with off-fault damage and constant pore pressure, we find that one major effect of off-fault damage is to relax the requirement of overlap between the two fault segments for rupture to propagate through a dilatational stepover. This suggests that when off-fault material is weak, a propagating rupture may jump a dilatational stepover without a significant overlap between the two fault segments. We remark that the extensive plastic yielding in the model of elastoplastic case is associated with a very week off-fault medium, such as the closeness CF of 0.633. When the off-fault material in dilatational stepover is stronger, the extent and magnitude of the plastic strain will be

31

smaller (Figure 2.10). Correspondingly, the PCS distribution will also be altered (Figure 2.11). In this set of models, we set off-fault material cohesion as 9.0 MPa, 20.0 MPa and 40.0 MPa for CF= 0.736, CF=0.556 and CF=0.385, whereas the example analyzed in elastoplastic case has the cohesion of 14.45 MPa for CF=0.633. All these cases are shown in Figures 2.10 and 2.11 for comparison. Notice that the PCS distribution from the model of CF=0.385 is very similar to that from the reference case (i.e., Figure 2.7(a)), as plastic yielding is very limited in this case (Figure 2.10).
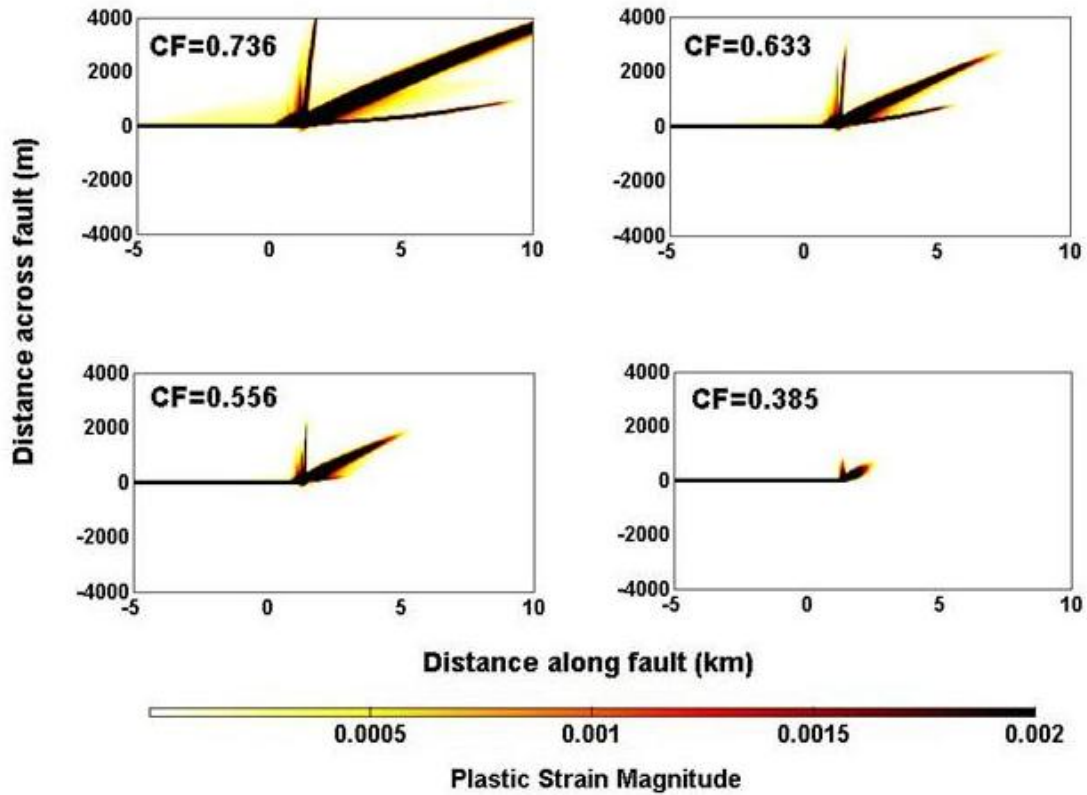
Figure 2.10 Plastic deformation at 14 s in the elastoplastic case with drained pore pressure, but different CF values.
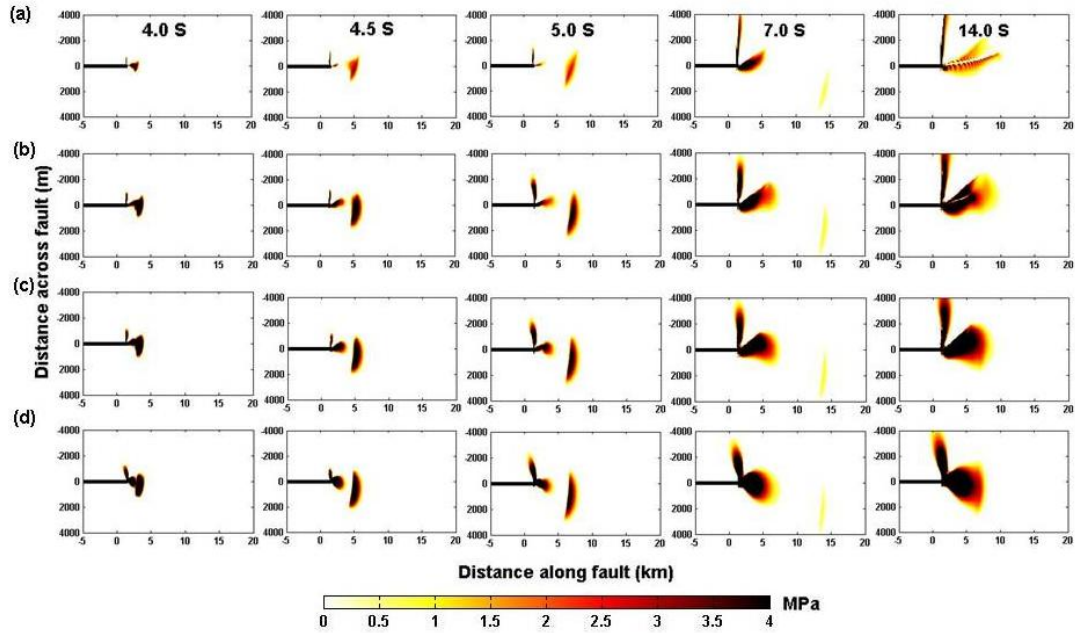
Figure 2.11 The history of the Positive Coulomb Stress (PCS) in the elastoplastic case with drained pore pressure, but different values of CF. (a) CF=0.736, (b) CF=0.633, (c) CF=0.556, and (d) CF=0.385.

Pore pressure changes in a stepover can significantly alter rupture behavior, particularly at a dilatational stepover. In the two cases of time-dependent pore pressure with an elastic or elastoplastic medium in the above section, the PCS region is hard to grow in the dilatational quadrant (Figures 2.7(b) and 2.7(d)) of the first fault. We remark that the value of B= 0.8 used in these models has been used in many previous studies (e.g., Rice and Cleary, 1976; Harris and Day, 1993; Duan and Day, 2010). However, there is not much observational evidence for one to choose the appropriate value of B. Integrating observations about rupture behavior of natural earthquakes at a stepover (e.g., Wesnousky, 2006) with theoretical studies of rupture dynamics of parallel faults

with a stepover may provide us with a means to place some constraints on the value of B in natural earthquakes. Observations (e.g., Wesnousky, 2006) show that it is common for a rupture to propagate through a dilatational stepover with a width smaller than or equal to 3~4 km. One possible explanation is the limitation of the 2D model, the real rupturing process is occurring in 3D and 2D model may not be able to capture all possible aspects, such as: two faults are not parallel anymore in a certain depth, or majority of the field observable stepovers are not bounded by two perfectly parallel faults; another possible explanation is the B value of 0.8 used in the above models and other previous studies (e.g., Rice and Cleary, 1976; Harris and Day, 1993; Duan and Day, 2010) may be the upper limit of the B value to give out a reasonable simulation result. In the extreme case, the poroelastic effect through B may not operate in natural earthquakes (i.e., B=0). Nevertheless, Wesnousky (2006) noticed that the number of observable dilatational stepovers is much larger than that of the compressive stepovers in his data set, i.e., six to one (Wesnousky, 2006). We believe this observation suggests that time-dependent pore pressure does operate in natural earthquakes. Increased effective normal stresses in a dilatational stepover due to reduced pore pressure would make pre-existing secondary fractures more difficult to be reactivated, and thus maintain the dilatational stepover, as linkage of the two main fault segments by secondary fractures is more difficult. On the other hand, decreased effective normal stresses due to increased pore pressure in a compressive stepover are effective in removing the compressive stepover by linking secondary fractures between the two main fault segments.

In addition, we also test some cases in which rupture on the first strike-slip fault to be stopped at different velocity in the elastic model. In those cases, we gradually increase the value of dynamic friction coefficient toward the end of first fault. By doing this, we could decrease the stress drop when propagating rupture approaches the first fault end. We find that the Positive Coulomb stress distribution is greatly influenced by the suddenness of the rupture being stopped at the first fault end. We use the last 1 km slip gradient to quantify the suddenness of rupture stopping at the fault end, as did by Elliott et al. (2009) in their field measurements. The general observation is that the area of PCS around the first fault end is proportional to the suddenness of rupture stopping. Furthermore, the maximum jumpable width of stepover has a strong correlation with the suddenness of rupture stopping which is characterized by the slip gradient of last 1 km from the fault end. We will discuss this topic in another paper.

3. COSEISMIC SLIP GRADIENT, RUPTURE COLLIDING VELOCITY AND

RUPTURE JUMP ON PARALLEL STRIKE-SLIP FAULTS

3.1 Introduction

The final rupture length in an earthquake occurred on a strike-slip fault has been regarded to be proportional to the magnitude of the event (e.g., Scholz, 2002). Geometrical discontinuities, such as stepovers, along fault strike act as the main barriers for the rupture propagation. Effects of stepovers on rupture propagation have been investigated from both field and theoretical points of view (Segall and Pollard, 1980; Schwartz and Coppersmith, 1984; Sibson, 1985; Harris et al., 1991; Harris and Day, 1993a; Wesnousky, 2006; Duan and Oglesby, 2006). Harris and Day (1993) numerically simulated the rupture behavior within two parallel strike-slip faults and found that the maximum jumpable stepover width is ~5km. The filed measurements from Wesnousky (2006) verified the crucial role stepovers play to stop rupture propagation and constrain the final rupture length and final earthquake magnitude. Oglesby (2008) first numerically explored the relationship between the form of rupture termination and the ability of the rupture to jump the stepover in a parallel strike-slip fault system. He points out the possible correlation between the slip gradient and the deceleration of the rupture front within the last several km of a rupture fault, which would control the rupture's ability to jump. After digitizing many published slip measurements on earthquake faults and calculated the slip gradient over the final several kilometers, Elliott et al.(2009) suggested a threshold value 20.0 cm/km in the last 1 km of the fault. If the slip decreases within the last 1 km at a slip gradient less than 20.0 cm/km, the rupture would have a

higher possibility to be stopped by the stepover even with a width less than 1 km. On the other hand, if the slip decreases within the last 1 km at a slip gradient larger than 20.0 cm/km, the opportunity of successfully jumping the stepover will be increased significantly. In this paper, we introduce a more complete version of the relationship between the slip gradient in the last 1 km and the maximum width of the jumpable stepover. In addition, we also examine how the colliding velocity, which is the rupture velocity at the end of the first fault in a parallel fault system, affects the slip gradient, and thus the jumping ability.

3.2 Model

We construct a simple 2D strike-slip faulting model shown in Figure 3.1 We use a finite-element computer program EQdyna (Duan and Oglesby, 2006; Duan and Day, 2008) to perform dynamic rupture simulation in this study. In our model, two left lateral strike-slip fault segments with a half length 14 km are embedded in a homogenous elastic medium. We primarily perform our calculations under an initial stress field: $\sigma_{11} = \sigma_{22}$= -33.3 MPa and σ_{21} = 20.0 MPa. In this initial stress field, the maximum compressive principal stress makes an angle of 45^0 with respect to the fault surface. The material and computational parameters are listed in Table 3.1. We build two models: model A and B. In model A, both faults are having the same friction parameters. In model B, we assign a smaller static friction coefficient on the second fault to lower the shear strength on it. We employ the convention that negative normal stress value means compression. Elliott et al. (2009) found that the slip gradient measured at the last 1 km has a notable threshold value 20 cm/km, under which the rupture can't successfully jump

a stepover even less than 1 km in width. In order to generate multiple slip gradients over

the last 1 km on the first fault,
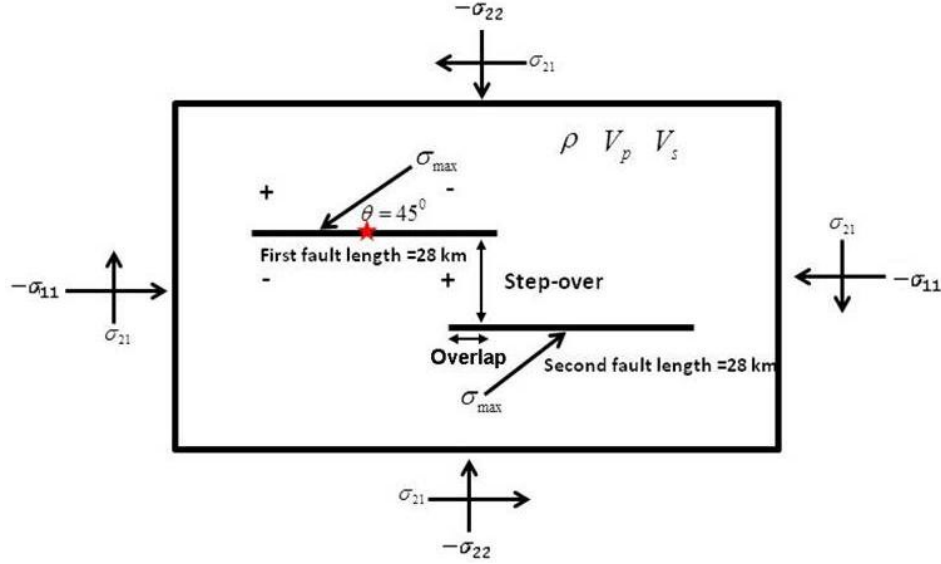
Figure 3.1 The model geometry, sense of slip and initial stress in our calculations. Two parallel left-lateral strike-slip faults are imbedded in a homogeneous elastic or elastoplastic medium. Compressional and dilatational quadrants around the first fault are labeled by plus (+) and minus (-) signs, respectively.

we linearly increase the dynamic frictional coefficient over the final several kilometers

of the first fault (Figure 3.2) in order to decrease the dynamic stress drop over that

distance. In each case, the rupture starts at the middle of the first fault and propagates at

a fixed velocity within a preset nucleation patch to allow rupture to gain enough energy.

Outside of the nucleation patch, rupture propagates spontaneously. We ensure that the

rupture successfully reaches the end of the first fault and check the slip gradient over

final 1 km distance. We also ensure different cases produce different slip gradients, and

those gradients evenly distribute over a range of 0 to 250 cm/km, which is the range of slip gradient over final 1 km distance in field measurements (Elliott et al., 2009). The corresponding parameters for each case have been listed in Table 3.2. In each case, we perform dynamic rupture simulations to find out the maximum jumpable width in both compressive and dilational stepovers.
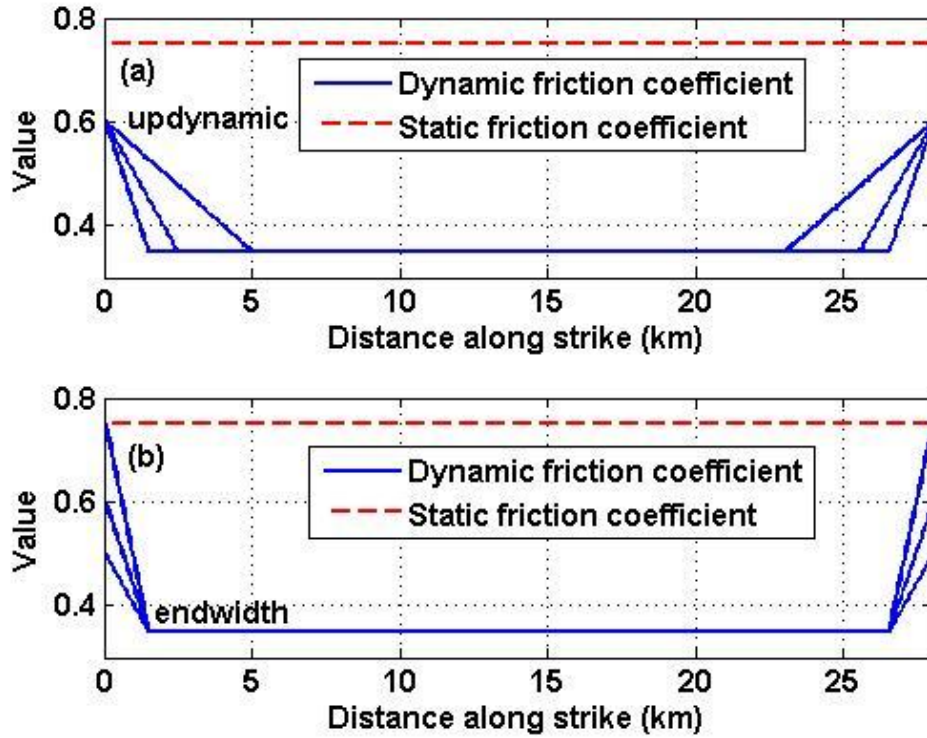
Figure 3.2 The static friction coefficient and dynamic friction coefficient distribution on the primary strike-slip fault. We linearly increase the dynamic friction coefficient from a point of several kilometers away from the fault end to the fault end. We use two methods for the linear increase: (a) the dynamic friction coefficient is fixed at the fault tip and the starting point of the increase is variable; (b) the starting point of the increasing is fixed and the dynamic friction coefficient at the fault tip is variable.

Table 3. 1 Material and computational parameters in model

Parameter	Value
Density	2700 kg/m^3
Vp	6000 m/s
Vs	3464 m/s
Initial normal stress: σ_{11}, σ_{22}	-33.3 MPa
Initial shear stress: σ_{21}	20.0 MPa
Static coefficient of friction	0.75 (model A), 0.70 (model B)
Original dynamic coefficient of friction	0.35

Table 3. 2 Friction parameter in different cases

Case #	Endwidth (km)	Updynamic	Slip gradient in last 1 km (cm/km)	Average stress drop (MPa)
1	12.5	0.70	51.0	2.01
2	10.0	0.70	73.8	3.27
3	6.5	0.75	93.7	4.86
4	5.0	0.75	112.0	5.66
5	5.0	0.70	123.4	5.81
6	3.5	0.75	136.1	6.47
7	5.0	0.60	143.6	6.11
8	2.5	0.75	155.4	7.00
9	1.25	0.75	186.4	7.67
10	0.50	0.75	198.9	8.08
11	0.0	0.75	236.8	10.01

* Endwidth is defined as the distance away the first fault end to linearly increase the dynamic friction coefficient. Updynamic is the maximum value the linear increment would reach at the last node on the first fault.

3.3 Results

We summarize the results of eleven cases of model A in Figure 3.3. It is clear that the maximum jumpable stepover widths are proportional to the slip gradient over the last 1 km of the first fault in both compressive and dilational stepovers: when slip gradient is 51.0 cm/km, the rupture could not jump over the stepover larger than 500 m, while when

slip gradient increases to be 236.8 cm/km, the jumpable width of stepover becomes over 5000 m. Elliott et al (2009) calculated the coseismic slip gradients over 25 field measured faults, and found that the slip gradient in the last 1 km of the first fault should be larger than 20 cm/km to be able to renucleate the rupture on the second fault. The x-axis intercepts in figure 3 are 26.37 cm/km for the dilational stepover and 24.59 cm/km for the compressive stepover, respectively, which are roughly comparable to the 20 cm/km observed by Elliott et al (2009). To understand what physical parameters may control the slip gradient near a stepover, we analyze the average stress drop on the first fault and the colliding rupture velocity at the end of the first fault. In Figure 3.4, we present the relationship between the slip gradient over the last 1 km distance and the average stress drop over the entire first fault from the eleven models, and the nearly linear relationship indicates a strong correlation between them. In these relatively uniform stress drop model (i.e., uniform stress drop along the majority of a fault), the average stress drop determines the maximum slip amplitude. Figure 3.5 shows the final accumulative slip distributions on the first fault in seven cases with different average stress drops. It is obvious that the case with the largest average stress drop 10.01 MPa has the greatest maximum accumulative slip; meanwhile, the case with the 2.00 MPa average stress drop has the smallest maximum accumulative slip. For faults with a given length, large slip amplitudes result in larger slip gradients near the fault ends. The slip gradient on a single fault surface has been reported to be the function of the maximum slip on a fault and the dimensions of the fault surface in a field study (Walsh and Watterson, 1988). The above model results are consistent with this field observation.

42
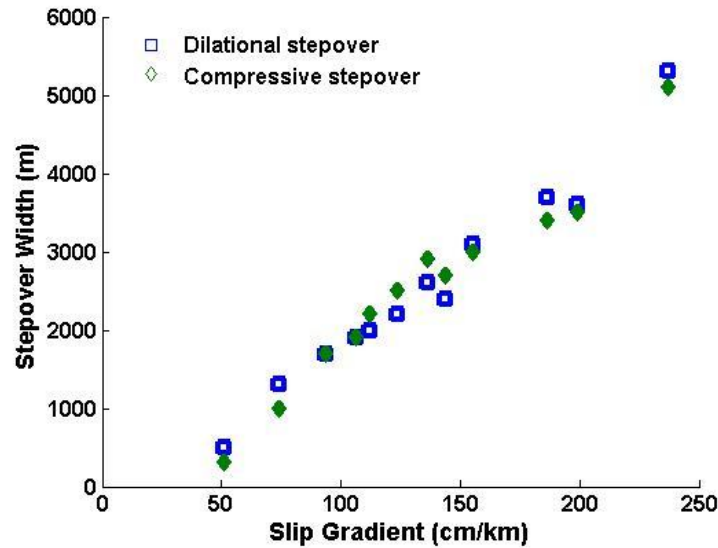
Figure 3.3 The maximum jumpable stepover width versus the slip gradient in the final 1 km of the first fault

Gradually decreasing stress drop at the fault end is expected to decelerate a rupture, leading to different colliding velocity at the end of the fault. Figure 3.6 shows the rupture time along the first fault for the above seven cases with different slip gradients. We find that rupture in the cases with smaller slip gradients (e.g., 51.00 cm/km and 74.80 cm/km) collides with the first fault end with a subshear velocity, while rupture in the cases with larger slip gradients collides with the first fault end with a supershear velocity.

43
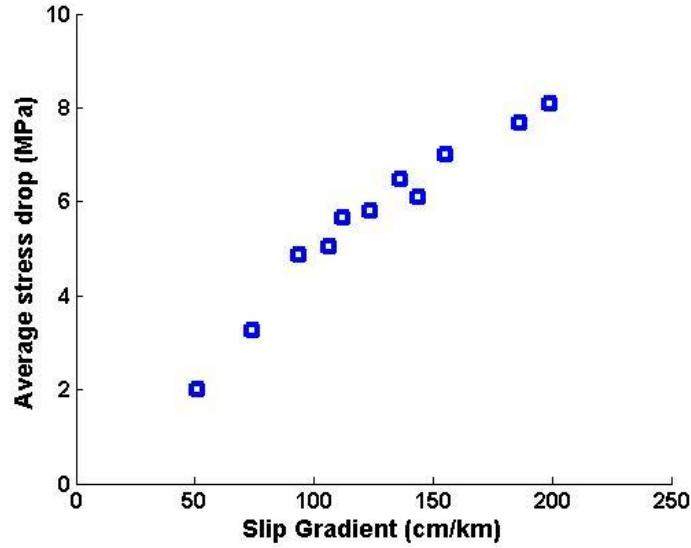
Figure 3.4 The Average stress drop in the first fault versus the slip gradient in the final 1 km of the first fault

3.4 Coulomb stress analysis on single fault tests

To understand why slip gradients at a fault end near a stepover dictate the maximum jumpable stepover widths, we examine the evolution of the stress field at the fault end using single fault tests. In particular, we examine the Coulomb stress variation after the rupture collides with the first fault end. The Coulomb stress is defined as $|\sigma_\tau| - \mu_s|\sigma_n|$; where σ_τ and σ_n are the shear stress and normal stress resolved on the parallel receiver fault, and μ_s is the static frictional coefficient.
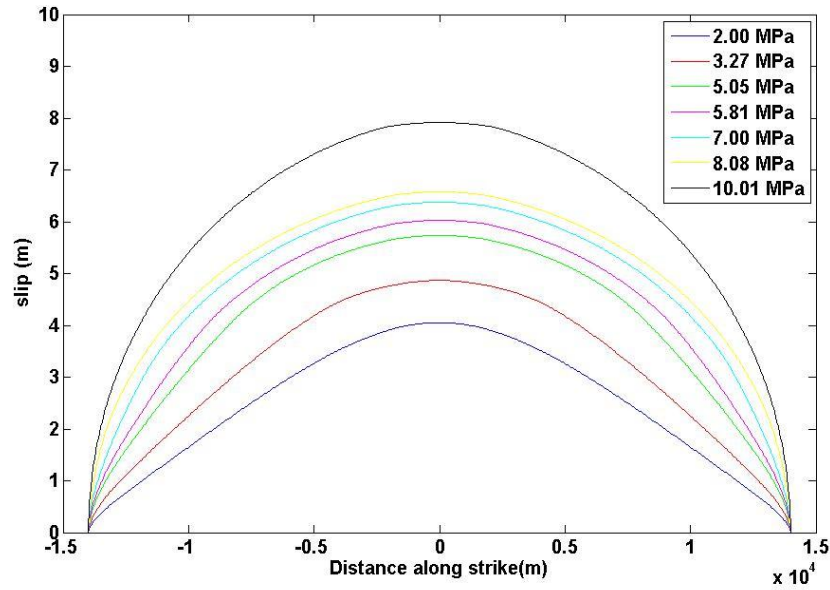
Figure 3.5 The final accumulative slip of cases with different slip gradient in the last 1 km. The cases we choose to display here are the same as the cases in figure 3.6
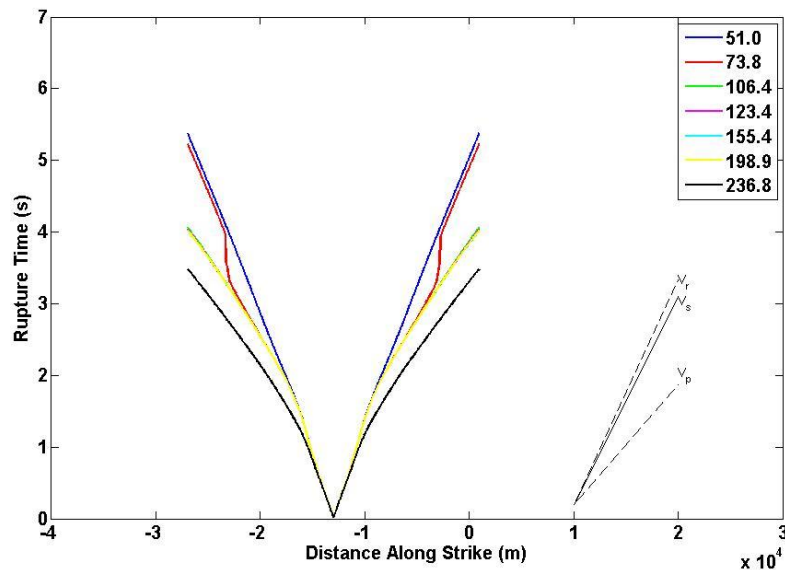
Figure 3.6 Rupture time along the fault strike for seven cases with different slip gradients (cm/km). V_r , V_s and V_p are the Rayleigh wave velocity, Shear wave velocity and the pressure wave velocity respectively.

45

We choose three cases with slip gradients of 50.0 cm/km, 155.4cm/km and 236.8cm/km to perform the Coulomb stress history analysis, which represent different average rupture velocities in Figure 3.7.
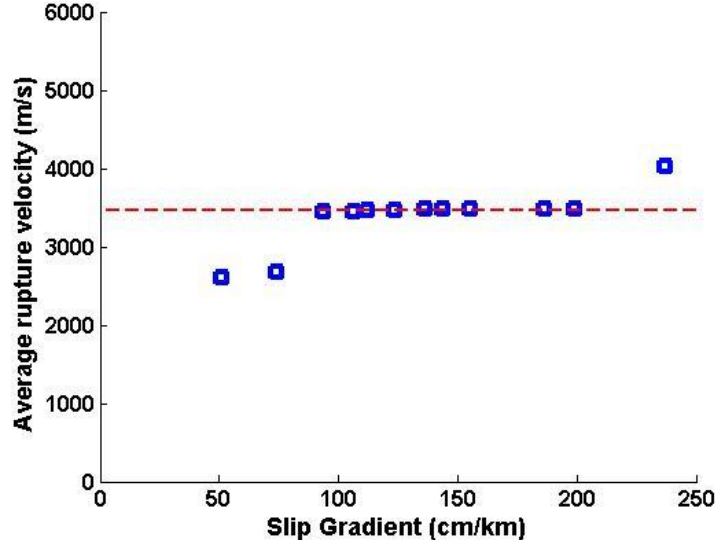
Figure 3.7 The average rupture velocity on the first fault versus the slip gradient in the final 1 km of the first fault. Here we define the average velocity as the result of the half fault length (14.0 km) divided by the time rupture needs to reach the fault end.

In the case with slip gradient of 50.0 cm/km, the rupture needs 5.375 S to propagate from the center to the tip of the first fault with an average velocity of 2.605 km/s, which is much smaller than the S-wave velocity in our model. Here we define the average velocity as the result of the half fault length (14.0 km) divided by the time rupture needs to reach the fault end. In Figure 3.8, we show the Positive Coulomb stress history around the first fault from 5 S to 14 S. After the rupture reaches the first fault end at 5.37 S, a

small patch of positive Coulomb stress can be observed, and in the following several

seconds the size of this positive Coulombs stress is in limited growth at the end of first

fault, which directly constrains the maximum width of jumpable stepover. At this slip

gradient, the corresponding rupture velocity is below S-wave velocity in the model, and

the low velocity also suggests the low dynamic stress drop during fault sliding.
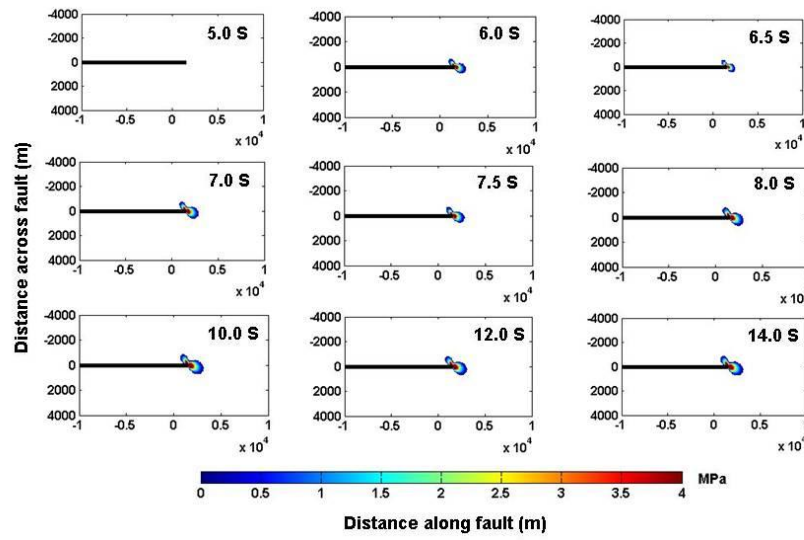
**Figure 3.8 The history of positive coulomb stress distribution on the first fault end
in the case of slip gradient 50 cm/km at first fault end in the single fault test.**

In the case with slip gradient of 155.4 cm/km (Figure 3.9), we use a relatively larger

average stress drop (Figure 3.4) than the above case to generate this slip gradient over

the final 1 km. Correspondingly, the average rupture velocity increases to the S-wave

velocity in our model. The Coulombs stress analysis indicates that, due to the relatively

larger rupture velocity, the positive coulomb stress has been intensified at the end of the

first fault, and the positive coulombs tress appears at 4.0 S. During the following times,

47

the positive coulomb stress keeps growing. At 5.0 S, a crescent shape splits away from the fault end and propagates into the compressive quadrant of the first fault. This crescent-shape positive coulomb stress remains in the following 2 seconds and disappears before 8 seconds, which constrains the largest jumpable width of parallel compressive stepovers.
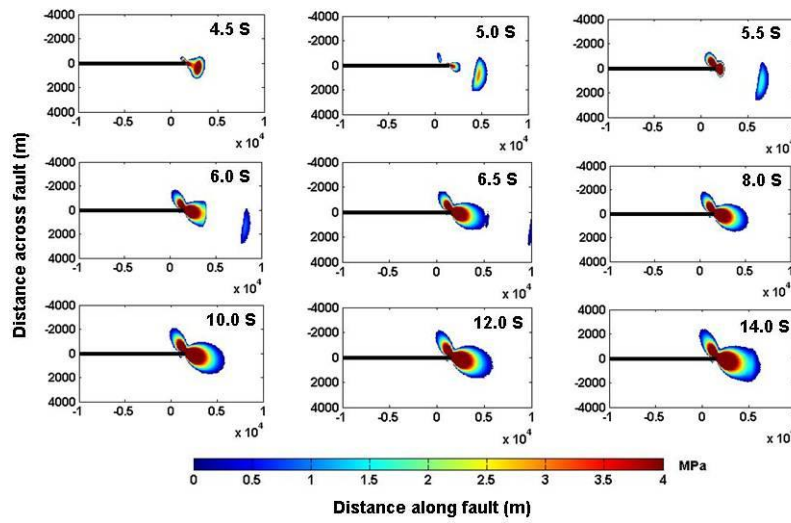
Figure 3.9 The history of positive coulomb stress distribution on the first fault end in the case of slip gradient 155.4 cm/km at first fault end in the single fault test.

In the case with slip gradient of 236.8 cm/km (Figure 3.10), the rupture has an even larger average rupture velocity, and arrives at the first fault end earlier than the previous two cases. The corresponding positive Coulomb stress has a larger extent around the first

fault end, and the split crescent positive coulomb stress has a bigger size, stronger

intensification and longer lasting time.
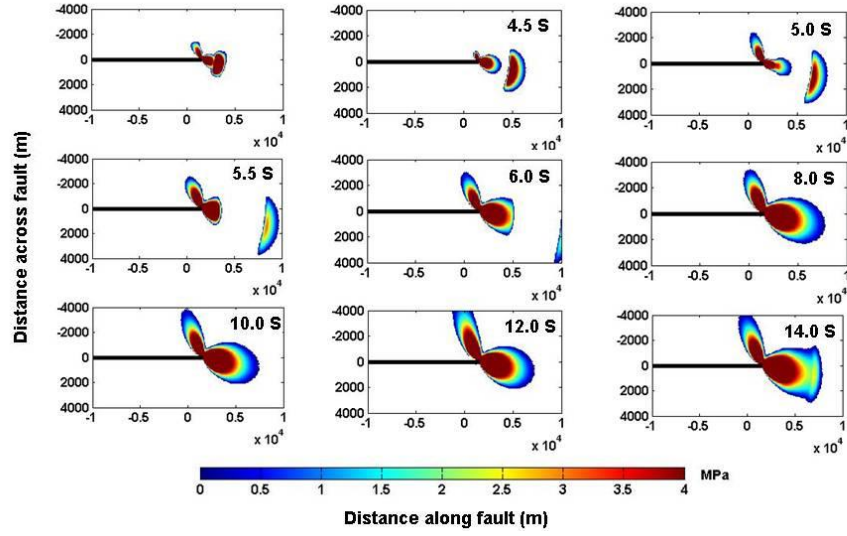
Figure 3.10 The history of positive coulomb stress distribution on the first fault end in the case of slip gradient 236.8 cm/km at first fault end in the single fault test.

3.5 Discussion

How rapidly the rupture stops at the fault end could determine the existence and

intensity of the stopping phase which has been regarded as the key factor to radiate

seismic energy (Bernard and Madariaga, 1984; Spudich and Frazer, 1984). The radiated

seismic energy can be the important parameter to trigger the rupture on nearby faults

(Oglesby, 2008). In Oglesby's research (2008), for the initial stress of the model, the

shear stress has been linearly decreased to 0 MPa at the last several kilometers (e.g., 0.1-

2.5 km) of the first fault and the shear strength remains unchanged. Under that initial

stress, the rupture decelerates just before colliding with the fault end. In our model, we

choose the method of linearly increasing the dynamic friction coefficient at the last

49

several kilometers of the fault. The rupture starts to decelerate roughly at the 7.0 km away from the fault end, and our method successfully generates multiple scenarios of rupture colliding with the fault end with different velocities. The sudden stop (or rapid deceleration) and gradual deceleration of rupture have totally different efficiencies in generating stopping phase (Oglesby, 2008). Here we find that even in cases with sudden stop only at the fault end, the larger colliding velocity (super-shear) and the smaller colliding velocity (sub-shear) also have obvious differences in seismic radiations around the fault end. Notice that the case with slip gradient of 236 cm/km is a homogeneous dynamic friction case, so we can compare other cases with this case in examining effects of rupture deceleration. We find that the colliding velocity at a fault end can significantly affect the jumping behavior in a stepover fault system. If the rupture collides with the first fault end at a supershear velocity (Figure 3.6), the intensity of the stopping phase will be increased greatly, which results in the generation of the split crescent positive Coulomb stress (Figure 3.8-3.10) in the compressive quadrant and a large positive Coulomb stress lobe in the dilational quadrant. Furthermore, the size and intensity of those positive Coulomb stresses are proportional to the colliding velocity and corresponding average stress drop.

In addition, Elliott et al (2009) noted a threshold value in slip gradient constraining the rupture's jumping ability. Our modeling results suggest a linear relationship between the slip gradient and the maximum stepover width that can be jumped. Figure 3.11 is the summary of the results from field measurements, the vertical red dash line is the threshold value proposed by Elliott et. al. (2009), and the blue dash line is the linear

50

relationship from our model. It is obvious that the linear relationship we propose does not outline the boundary of dividing the jumpable and unjumpable stopovers found by Elliott et al. (2009). Many reasons can contribute to this difference. The first one would be the simplifications in our model. In both faults, we assign the same initial stresses and the same friction coefficients, which may not be the case in real earthquake faults. Our preliminary simulation in model B with a lower static friction coefficient ($\mu_s =0.7$) indicates that a lower initial shear strength would increase the rupture's jumping ability on it in the model with the same slip gradient on the first fault. In figure 3.11, we could observe that the line from model B has a larger slop compared with the line in case A, which means that the linear relationship we find only exists under a specific set of model configuration. Second cause would be the fault length. In our model, we fix the half length of the strike-slip fault to be 14 km, which is approximately the seismogenic depth for many strike-slip faults (Ruth and Day, 1993). Meanwhile, in Elliott's research, the measured length of fault trace could vary from 2~3 km to more than 40 km. We know under the same stress drop, the smaller ruptured fault length would give out a smaller slip gradient near the tip, but the seismic rupture on them may have the same jumping ability to stopovers. As we know a longer ruptured fault length indicates a larger propagation time of the rupture, which can generate a larger slip gradient.
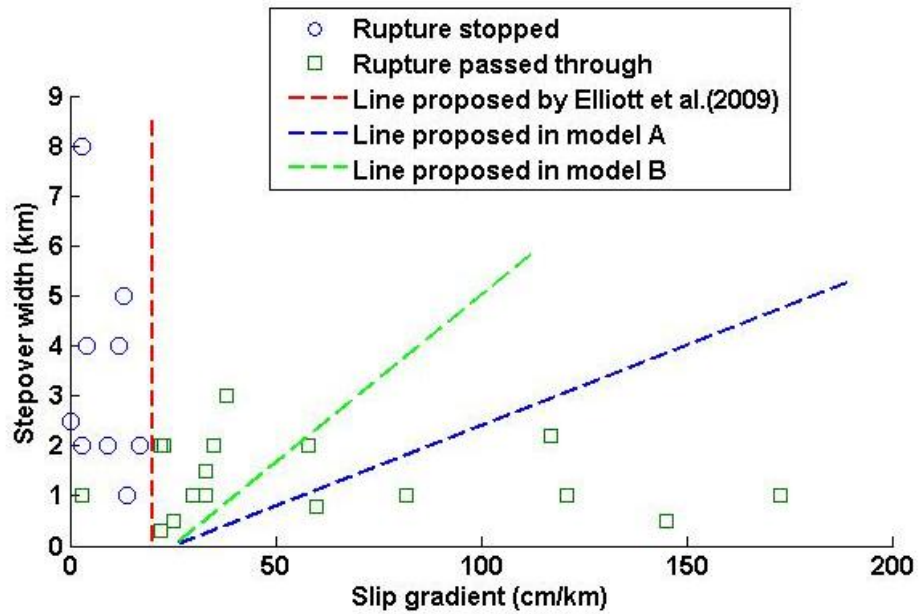
Figure 3.11 Comparison of the dividing line from filed measurements by Elliott et al. and the lines generated by the models. The red dashed line represents the possible dividing line proposed by Elliott et al., (2009). The green dashed line and blue dashed line are the linear relationships between the slip gradient and the maximum width of stepover jumped by the rupture in mode A and B, respectively.

4. MULTI-CYCLE DYNAMICS OF THE AKSAY BEND ALONG THE ALTYN TAGH FAULT IN NORTHWEST CHINA

4.1 Introduction

Fault geometry could greatly affect the earthquake rupturing process, especially the geometrical irregularities, such as: stepover, bend and branching. Harris and Day (1993) numerically examined the effect of stepover imposing on the fault system with two parallel strike-slip faults. Duan and Day (2008) tested the effect of a fault kink (sudden strike change) within a model with off-fault inelastic deformation. The rupture dynamics of branched fault geometry have also been discussed, either with no material contrast (e.g., Aochi et al., 2000; Oglesby et al., 2003; Duan and Oglesby, 2007) or with material constrast (DeDontney et al., 2011). Oglesby (2008) pointed out the correlation between rupture stop suddenness and the maximum jumpable stepover width. In the field research of the geometrical irregularities, Wesnousky (2006) measured 22 historical strike-slip earthquakes with length ranging 10 to 420 km and found that nearly two thirds of the measured stepovers with 3-4 km width or lager functioned as the barrier to the propagating rupture. Elliott et al. (2009) measured the slip gradient at the final several kilometers on faults and proposed the possible relationship between the slip gradients and the ability of rupture to jump the geometrical stepover at the fault end. In addition, earthquakes usually keeps occurring on large faults, for example, the San Andreas Fault in California, and Longmen Shan fault in Sichuan, China. The repeat of earthquake on the same fault would greatly vary the stress condition on the fault, in particular at geometrical irregularities, and thus affect the seismic rupturing process. Sagy et

al.(2007), employed new laser-based methods to measure exposed fault surface ranging from 10 um to 120m, and provided a first-hand measurement of the variation of fault surface roughness with increasing accumulative slip or repetitive earthquake rupture events. Chester et al.,(1993) have noted the microstructure leading a low frictional strength of San Andreas Fault could be the result of repeated rupturing event and fault maturing process. Duan and Oglesby (2006, 2007) modeled the rupture behavior within the parallel strike-slip faults and branched fault system under a heterogeneous fault stress from prior earthquakes.

Previous rupture dynamic research is usually carried out on the simplified and regular fault geometry. The roughly 200 km long Aksay bend is a restraining double-bend and stepover within the active left-lateral Altyn Tagh fault in northwest China outlining the northern boundary of Tibet Plateau (Figure 4.1). In this study, we use a multicycle earthquake simulator developed by Duan and Oglesby (2006) to explore how the complex fault geometry would affect the stress accumulation and relaxation within the Aksay double-bend and how the stress heterogeneity would constrain the rupture interaction within the Aksay double-bend.

4.2 Method

The viscoelastic model proposed by Duan and Oglesby (2005) has been employed to simulate the interseismic loading period. A finite element code (EQdyna) developed by Duan and Oglesby (2006) is used to simulate the seismic rupturing process. I discuss each of them in this section.
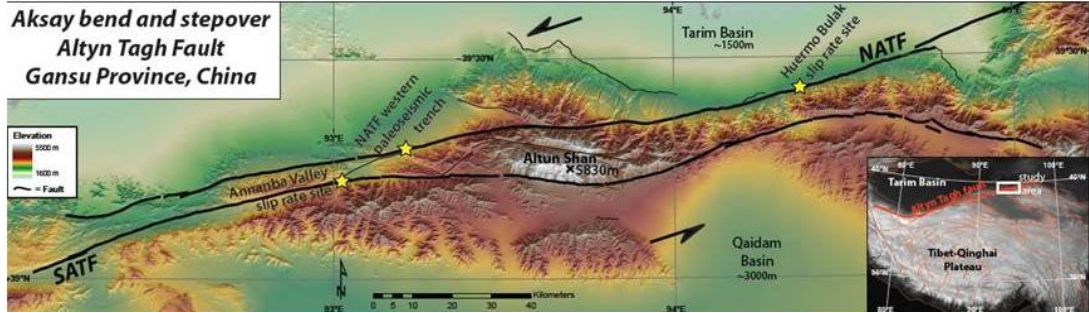
Figure 4.1 Topographic map of the Aksay bend and its location on the Atlyn Tagh fault. NATF and SATF are northern and southern strands, respectively. The black arrows represent the loading direction on both sides of the ATF, and the three yellow stars are the locations where the paleoseismic trenches have been investigated by our collaborators.

4.2.1 Linear viscoelastic model for the interseismic period

The interseismic loading process has been represented by a Maxwell viscoelastic model. The stress loading and relaxation process on the fault are corresponding to the spring elastic loading and the dashpot viscous relaxation in the conceptualized Maxwell viscoelastic model. We allow the system to adjust the shear and normal stresses on a fault segment at time t in the interseismic period according to the equations proposed by Duan and Oglesby (2005):

$$\sigma_\tau(t) = (\sigma_\tau^0 - \omega\gamma_\tau)\exp\left(-\frac{\mu}{\omega}t\right) + \omega\gamma_\tau \tag{4.1}$$

$$\sigma_n(t) = (\sigma_N^0 - \omega\gamma_n)\exp\left(-\frac{\mu}{\omega}t\right) + \omega\gamma_n \tag{4.2}$$

55

where μ is the shear modulus, ω is the viscosity, γ_τ and γ_n are strain rates resolved onto the normal and shear directions of the fault plane.

4.2.2 Conceptual understanding on the viscoelastic loading in the interseismic period

In order to understand the features of the viscoelastic model of interseismic loading, we use the Mohr circle analysis to analyze the elastic effect of increment on both shear stress and normal stress with different angles between the strike and the pure-shear loading direction. As the relaxed amounts on both normal and shear stresses are just limited portions of the elastic loadings within the loading time of several hundred years. The variation of the strike in ATF system ranges from 0^0 to nearly 45^0 with respect to the loading direction. In elasticity, strain and stress are interchangeable by using Hook's law, so we could discuss it in the stress domain. Figure 4.2 is the Mohr circle representation of the pure shear environment. We use the convention that the compressive stress is the positive value and the dilatational stress is the negative value. The x and y axes are normal and shear axes respectively. Then the loading direction is along the y-axis (shear stress axis). We define θ as the angle between the loading direction and the strike direction in reality (we assume the strike has the same positive direction as the loading), and then the angle 2θ is the angle measured clockwise from the loading axis to the strike axis in Mohr circle. In this conceptual model, we assume the initial normal and shear stresses are zero, then we load the system under different θ value. It is obvious that when $\theta = 0^0$, which means the strike direction is parallel to the loading direction, the loading only works on the shear direction and no effect on the

normal direction. In Figure 4.3, when $2\theta = 90^0$, which means the strike direction is 45^0 with respect to the loading direction in reality, only the normal direction will be loaded. When $2\theta = 45^0$ the loading will impose equal amount of increments on both the normal and shear directions. When $0^0 < 2\theta < 45^0$ there is more amount of loading on the shear direction than the normal direction. When $45^0 < 2\theta < 90^0$ more normal direction loading will be imposed compared with shear direction. Meanwhile, the viscous effect is also closely related with θ due to the equations: $\gamma_n = \dot{\varepsilon}\sin(2\theta)$ and $\gamma_\tau = \dot{\varepsilon}\cos(2\theta)$. Because the strain rate $\dot{\varepsilon}$ is constant in one certain case, the θ has a nonlinear relationship with the stress relaxation on both the normal and shear stresses. Therefore, the two competing factors: elastic loading and viscous relaxation make the final viscoelastic effect on normal and shear stresses to have a non-linear relationship with θ, which enriches the heterogeneity. We think the variation of θ along strike is the main cause to the final stress heterogeneity on both strands of ATF after the first interseismic loading and in the following cycles.
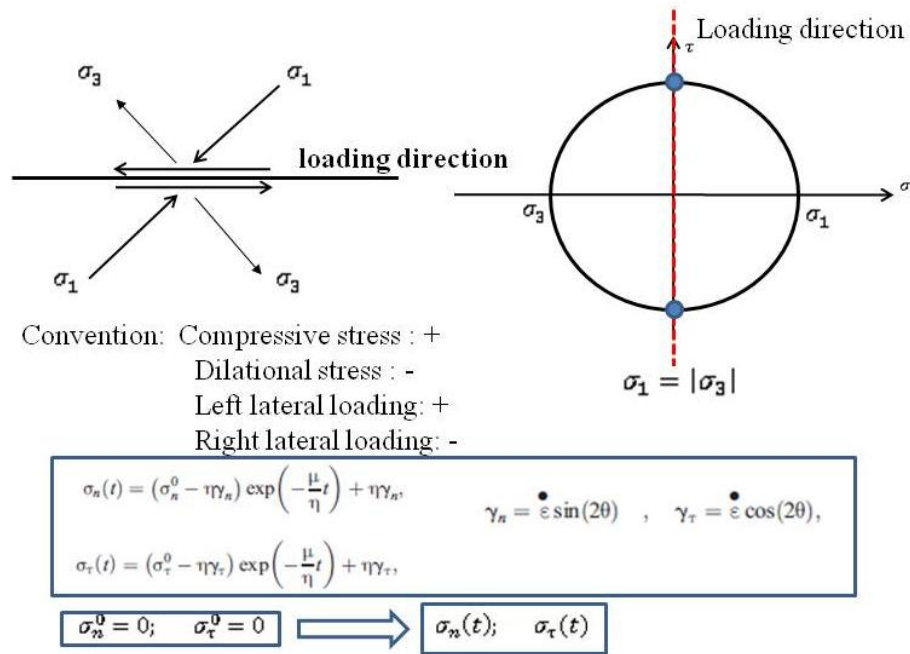
Figure 4.2 The conceptual model and the corresponding Mohr circle. In the conceptual model, we assume the original normal and shear stresses are zero.
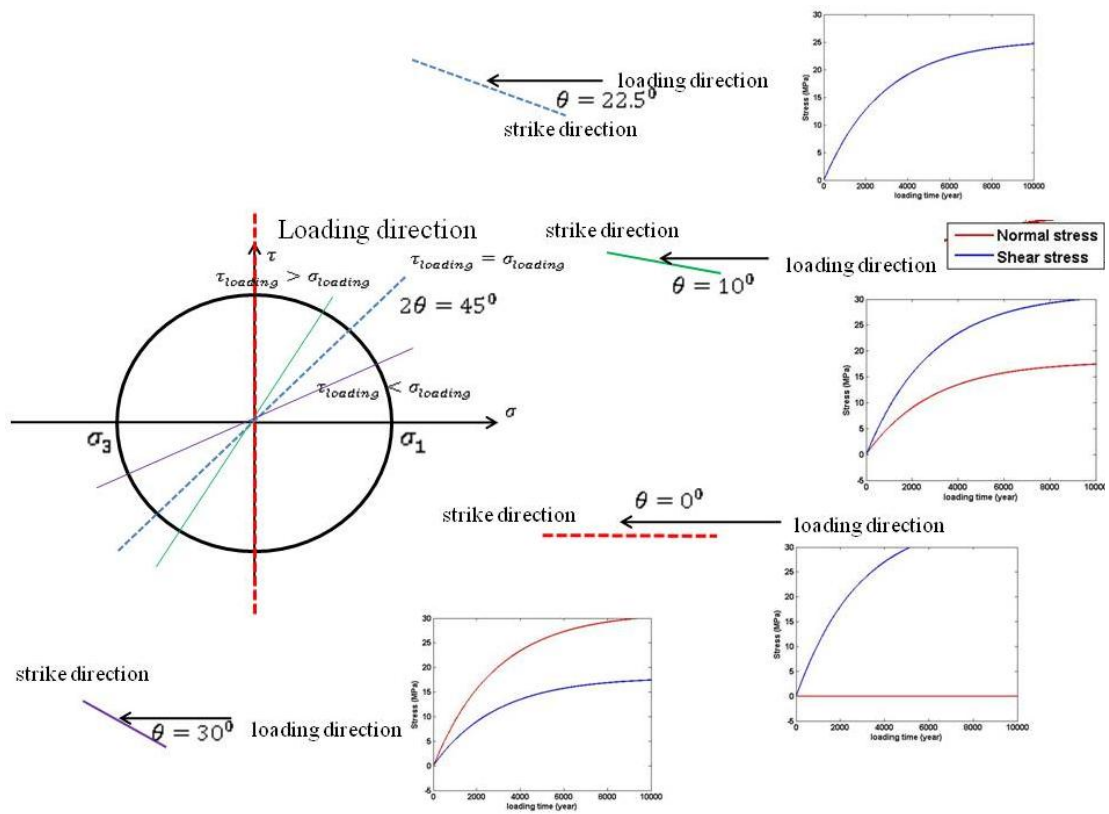
Figure 4.3 Analysis of the effect on stresses of the angle between the loading direction and the strike.
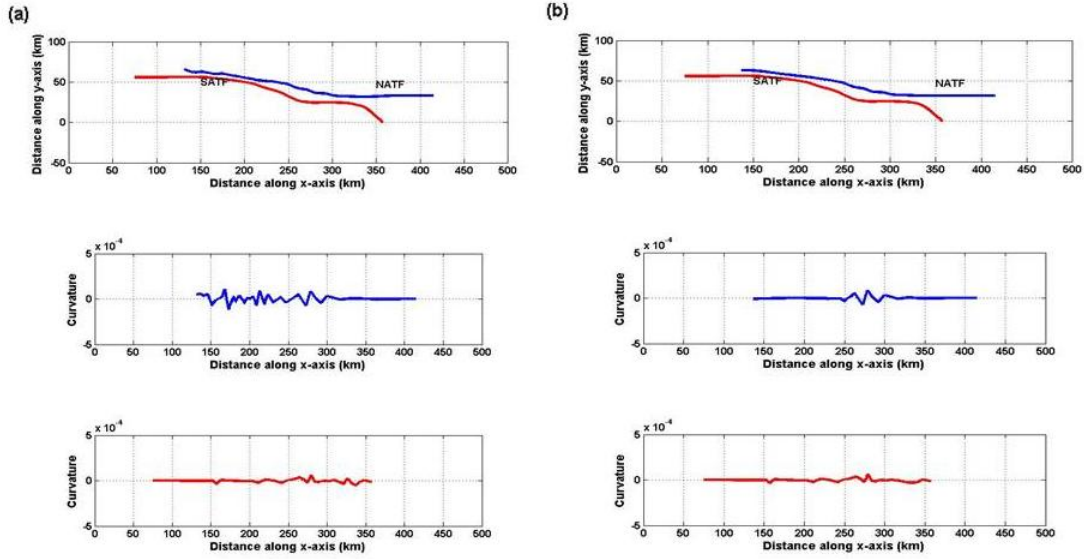
Figure 4.4 (a) the interpolated fault geometry of the Aksay bend based on the measured controlling points and the corresponding curvatures on both strands. (b) the smoothed version of the fault geometry in (a) and their corresponding curvatures on both strands.

4.2.3 The model geometry

The surface trace of Aksay double-bend in Altyn Tagh fault system has been measured by our collaborators at UC Davis. 29 and 17 controlling points have been measured along SATF and NATF respectively, from geological maps. We use the limited controlling points to generate complete fault geometry by employing the natural cubic spline interpolation method. We assume the lithostatic stress in the model to be 50.0 MPa, which is corresponding to the depth of 3.0 km if the local lithostatic gradient is 25.0 MPa/km. It is assumed that the fault should have a smoother fault surface at the depth of 3.0 km than near the earth surface. So the interpolated fault trace was

60

smoothened (Figure 4.4(a)) to have a more even fault geometry (Figure 4.4(b)). The amount of smoothening operation has been quantitatively shown by using the concept of curvature, and the segment of NATF inside of the double-bend has been more strongly smoothened compared with the corresponding segment in SATF. We put the smoothening mainly on the bend part of NATF, because it has larger curvature values compared with other segments of NATF and SATF and those relatively small "bumps" (1-5 km) in curvature along fault strike would results in multiple locations of nucleation in our simulations, which is rarely observed in natural earthquakes.

4.2.4 Multi-cycle simulation process

A complete earthquake cycle consists of the interseismic loading process and the seismic rupturing process in our multi-cycle model. We have two separate components in our code to simulate the two processes. A homogenous initial stress outside of the nucleation patch has been assigned to the two fault strands before the first interseismic loading process starts. Then the interseismic loading follows the linear viscoelastic model according to equations (4.1) and (4.2). A presetting nucleation patch, within which a pre-existing initial shear stress (10 MPa) has been assigned, experiences the visoelastic loading too. We choose a nucleation patch size L_{nucl} somewhat larger than the critical value L_c which is able to sustain the dynamic instability (Palmer and Rice, 1973): $L_c = \frac{16}{13} \frac{\mu G_c}{(\tau_c - \tau_d)^2}$, Where μ is the shear modulus, G_c is the fracture energy, and the assumed Poisson's ratio is 0.25, τ_0 and τ_d are the static and dynamic friction coefficients respectively. When there is one node reaching the shear failure criterion, the interseismic loading is terminated and then a presetting 2.0 MPa would be added to the

shear stress on the nodes within the presetting nucleation patch. The shear and normal stresses at this moment are used as the initial stresses for following the dynamic rupturing simulation. After the completion of dynamic rupturing process, the frictional coefficient is reset to the static value and the first-cycle is finished. Then the second-cycle interseismic loading process starts by utilizing the residual stresses of dynamic rupturing in the first cycle, which is followed by the second-cycle dynamic rupturing process. Between each cycle, we neglect the geometry evolution, which means that we keep using the same mesh to implement dynamic rupture simulation in each cycle. Due to the relatively short time length of the simulation (< 1,500 years), the fault geometry has been assumed that no obvious change occurred.

4.2.5 Slip-and-rate weakening friction in dynamic simulation

We combine a slip weakening law (e.g., Ida, 1972) and a rate weakening law (Cochard and Madariaga, 1994; Shaw, 1995; Nielsen et al., 2000) as the main friction law in our model for dynamic rupture simulations.

$$f = \begin{cases} f_s - (f_s - f_d)^{\Delta u}/D_0 & \Delta u \leq D_0 \\ f_d & \Delta u > D_0 \ or \ \dot{\Delta u} > V_0 \\ f_{restren} - (f_{restren} - f_d)^{\dot{\Delta u}}/V_0 & \dot{\Delta u} \leq V_0 \ and \ \Delta u > D_0 \end{cases} \qquad (4.3)$$

where f_s and f_d are static and dynamic friction coefficients, $f_{restren}$ is the restrengthened friction coefficient after the sliding stops. D_0 and V_0 are critical slip distance and critical velocity, respectively. In this friction law, before the slip reaches the presetting critical distance, the friction follows slip weakening law. After the slip distance is larger than the critical distance and the slip rate falls below the critical

velocity, the friction follows the rate weakening law. By using this friction law, we could incorporate the frictional healing process, which has been widely observed in seismic inversions and rock deformation experiments.

Table 4. 1 Model parameters

Parameter	value
Loading rate	1.8 $\mu rad/yr$
Equilibrium (ambient) stress	50.0 MPa
Initial normal stress	50.0 MPa
Initial shear stress	0 MPa
Viscosity	$1.8, 2.0, 2.2, 2.4 \times 10^{21}$ Pa S
Shear modulus	2.2×10^{10} Pa
Possion's ratio	0.25
Density	2670 km/m^3
Static frictional coefficient	0.6
Dynamic frictional coefficient	0.5
Critical slip weakening distance D_o	0.2 m
Fault element size	200 m
Critical nucleation length	2.0 km

4.3 Results

In this section, we will first report the case of the preferred model, in which we will introduce the evolution of normal stress and shear stress, the event patterns over multi-cycle earthquake simulations, and the statistic analysis of the effectiveness of the Aksay double-bend in stopping or trapping the earthquake ruptures. Then, we report results of models with variations in model parameters, particularly in viscosity.

4.3.1 Results of the preferred model

We have several criteria used to choose our preferred model. First, the value of maximum slip should be smaller than 10 meters. There are many existing filed measurements of the surface slips and inversed slip distributions of certain earthquakes at depth, which could lend supports to the constraint of maximum 10 meters we set up on the simulation results. The field measurement of the seismic slip on earth surface in Wenchuan earthquake occurred in China, 2008 (Xu et. al., 2009), indicates that the total slips on the fault are less than 7.5 meters. In the 1992 Landers earthquake, the surface slip was variable averaging 2 to 3 meters over much of the rupture (Ponti, 1993; Sieh et al., 1993) . Two clear peaks in the slip distribution were observed, a southern peak on the northern part of the Johnson Valley fault and a broader northern peak on the Emerson and southern Camp Rock faults. Peak surface displacements of 6 meters were measured along the Emerson fault. (e.g., kanamori et al, 1992). Therefore, the common seismic slip expression on earth surface is roughly 2~7 meters. In our simulations, we set the lithostatic pressure in our model to be 50.0 MPa, which is corresponding to the depth of 2-3 km if we assume the local lithostatic gradient is 22-26 MPa/km. Therefore, we

could expect a somewhat larger maximum seismic slip than 2~7 meters. So we choose 10 meters as the upper limit in our simulations. Second, we set a constraint on the maximum seismic stress drop. The typical stress drop determined empirically from inversion of the radiated seismic waves are typically in the range 0.3 ~ 50 MPa with the median stress drop of 4.0 MPa (e.g., Allmann and Shearer., 2009). In our simulations, we make the stress drop in our model be no more than 5 MPa, which is within the empirical range and corresponding to the maximum slip we set up for the model.

4.3.1.1 Stress evolution and event pattern

In the preferred model, we use the parameters listed in table 4.1 and the viscosity is 1.8×10^{21} Pa S**.** Figure 4.5 shows the stress evolution during the interseismic loading of the first interseismic period. It is the stress evolution from a homogenous preset initial stresses to a heterogeneous stress distribution just before the first seismic rupturing event occurs. It has the largest stress variation and forms the basic pattern for the following stresses evolution. In this first cycle, we have a limited size of preset nucleation patch roughly in the middle of the planer segment on SATF, which is the spike of initial shear stress before the first cycle loading. With the increment of loading time, the stress becomes strongly heterogeneous due to different angles between the strike direction and loading direction along the fault strike. Several features could be observed: firstly, both the shear stress and normal stress have been increased except the normal stress on the segment parallel to the loading and shear stress on the segment having 45^{0} with respect to loading. On SATF, the positions at roughly 250 km and 350 km have large difference between the shear strength and the corresponding shear stress, which make it hard for

rupture to nucleate at or propagate through the two positions. On NATF, the segments with larger strike variations experience stronger stress heterogeneities after the loading.

The angle between the strike and the loading direction could give a good explanation to the above stress features in the loading of first earthquake cycle. In Figure 4.5 (a), at the starting moment, we assume there is only the 50.0 MPa lithostatic stress on the fault surface and no shear stress exists on it. We choose three points on the SATF to check the stress evolution, and they have the angles of 0^0, 22.5^0 and 45^0 with respect to the loading direction (Figure 4.6). At point a, due to the roughly parallel between the strike and loading direction, so only shear stress has been loaded and the shear strength keeps unchanged. At point b, the angle between the strike and the loading direction is about 22.5^0, the loading system would impose roughly equal amount increment on both the shear direction and the normal direction, which make the stress difference between the shear stress and shear strength almost unchanged compared with the starting moment, which make this segment become "locked". At point c, the angle becomes nearly 45^0, which means that only the normal direction would be loaded and no shear stress increment.

Figure 4.7 (a) illustrates the stresses at the starting moment of the coseismic rupture from event # 1- #10 on both SATF and NATF with a viscosity of 1.8×10^{21} $Pa\,s$ in interseismic loading. The predominant feature is the three segments favoring rupture initiation. Two segments are on the SATF, which are the relatively parallel to the loading direction. One segment is on the NATF. Those three segments have strikes roughly parallel to the loading, so they are rupturing-favored segments. Another feature
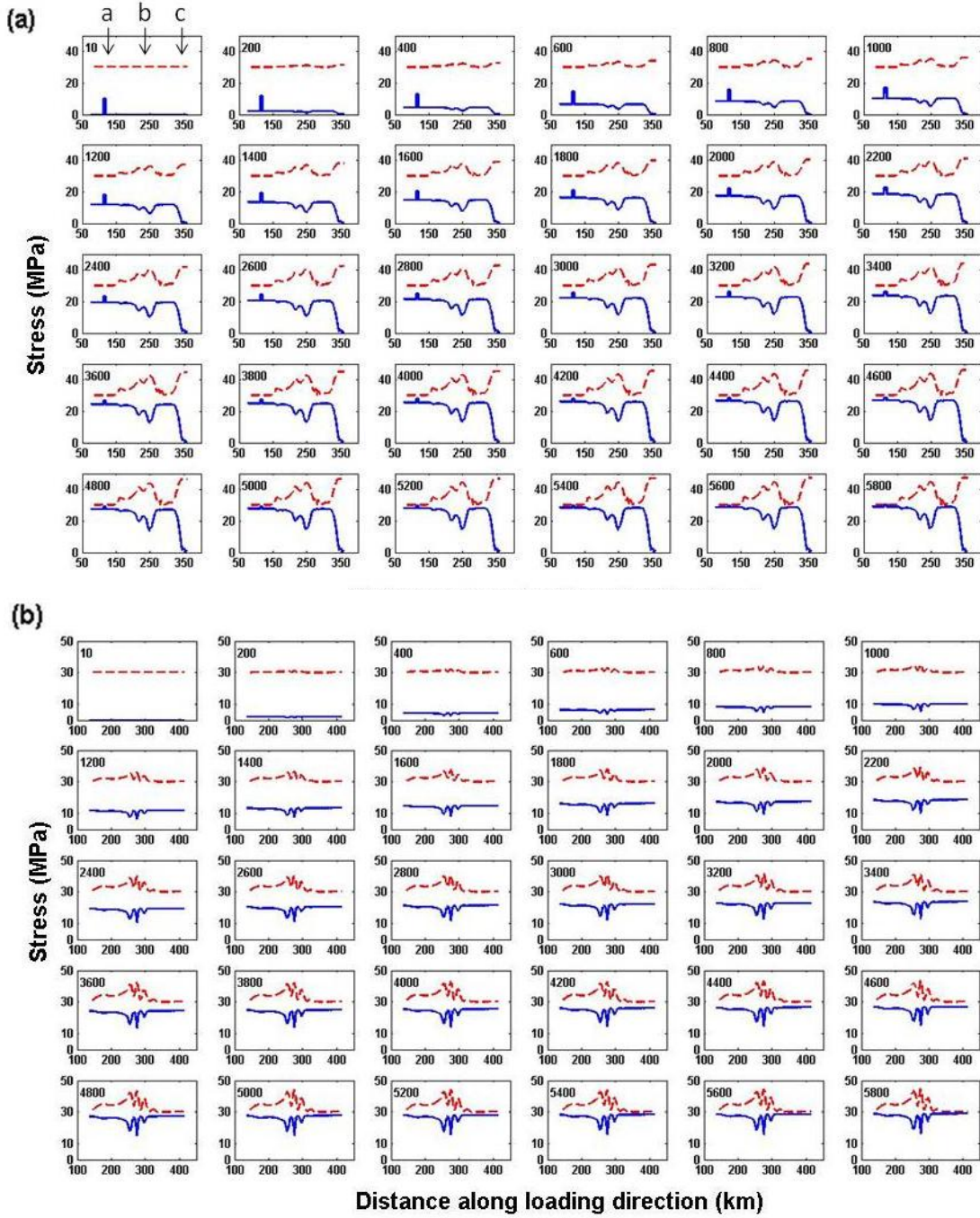
Figure 4.5 The evolution of shear stress and shear strength on the SATF (a) and NATF (b) during the intersesimic process in the 1st event. The dash line is the shear strength and the solid line is the shear stress. The number inside is the interseismic loading time (years).

is the alternative rupturing among the three favored segments in Figure 4.7 (b). The left planar segment in SATF is ruptured firstly due to the preset shear stress touches the strength within the nucleation patch. At the same time, the other two segments still need loading to reach failure. After the second cycle interseismic loading, one point in the planar segment of the NATF firstly fails then nucleates and rupture propagates bilaterally along the strike. After 14 seconds the right segment on the SATF is ruptured too. In the third cycle, only the left planar segment on the SATF ruptures again, which allows the rest two planar segments to regain the stresses to nucleate. In the fourth cycle, the rupturing repeats as the rupturing in the second cycle. In the following cycles # 5, 6 and 7, the rupturing sequentially occurs on the left planar segment of SATF, right planar segment and the planar segment on the NATF. Then cycle # 8, 9 and 10 repeat the rupturing cycle from # 5 to 7 (Figure 4.7(b)). Due to the slip and rate weakening law, the residual shear stress becomes oscillatory after the seismic rupturing process, which is a feature of friction laws that involve rate dependence.

Figure 4.8 is the complete representation of the coseismic slip of the one hundred earthquake cycles. Eight repeated event patterns could be observed: 1. Slip only occurs on the planar segment outside of the double-bend on SATF, which takes up to 34% of all events; 2. Slip only occurs on the planar segment outside of the double-bend on NATF, which accounts for 12% of the total; 3. Slip occurs on both the planar segment outside of the double-bend on NATF and the planar segment within the double-bend on SATF, which accounts for 20% of the total; 4. Slip occurs on both the planar segment outside of the double-bend on SATF and the segment within the double-bend on NATF, which

takes only 2%; 5. Slip occurs on the entire SATF except the locked segment, which takes

3%; 6. Slip only occurs on the planar segment of the SATF within the double-bend,

which takes 15%; 7. Slip occurs on the entire "unlocked segment" of the SATF and the

planar segment on NATF outside of the double-bend, which takes 6%; 8. Slip occurring

on both strands outside and within the double-bend takes 2% of all of the events.
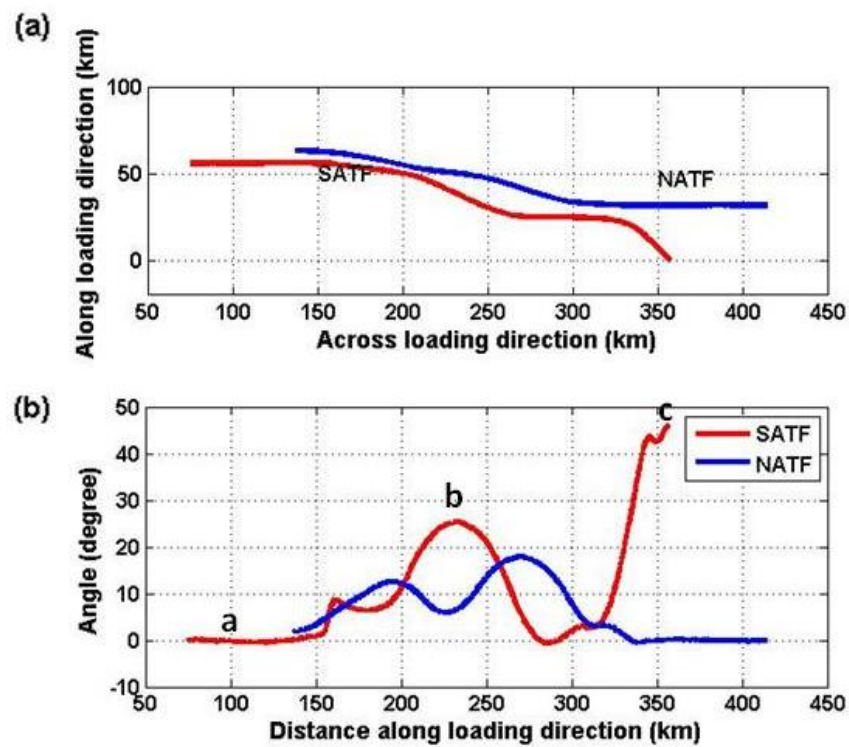
Figure 4.6 (a) the interpolated fault trace; (b) the acute angle between the strike and the loading direction.
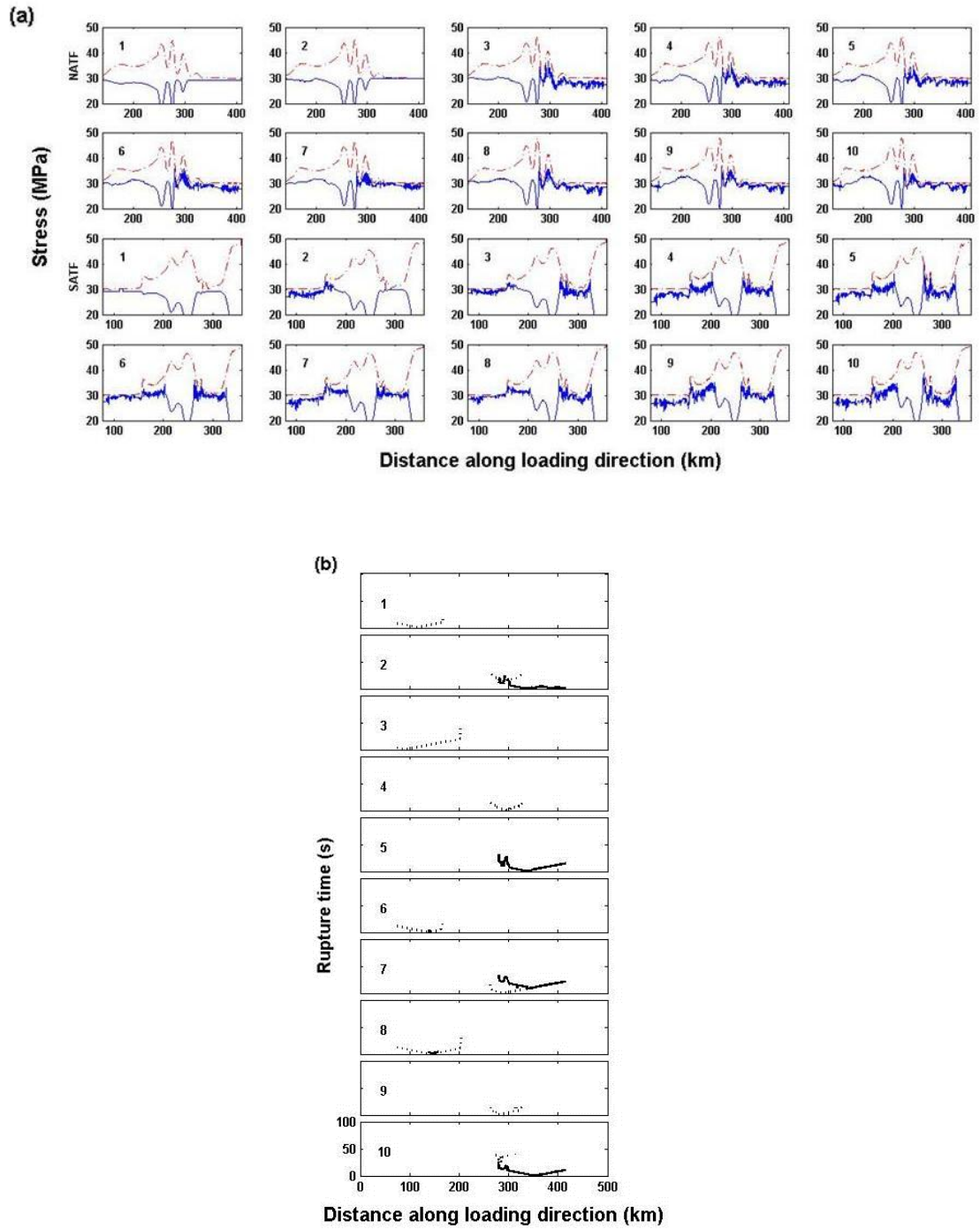
Figure 4.7 (a) The initial stresses of coseismic process in event #1~ 10 on both SATF and NATF; (b) Rupture history of the first ten events.
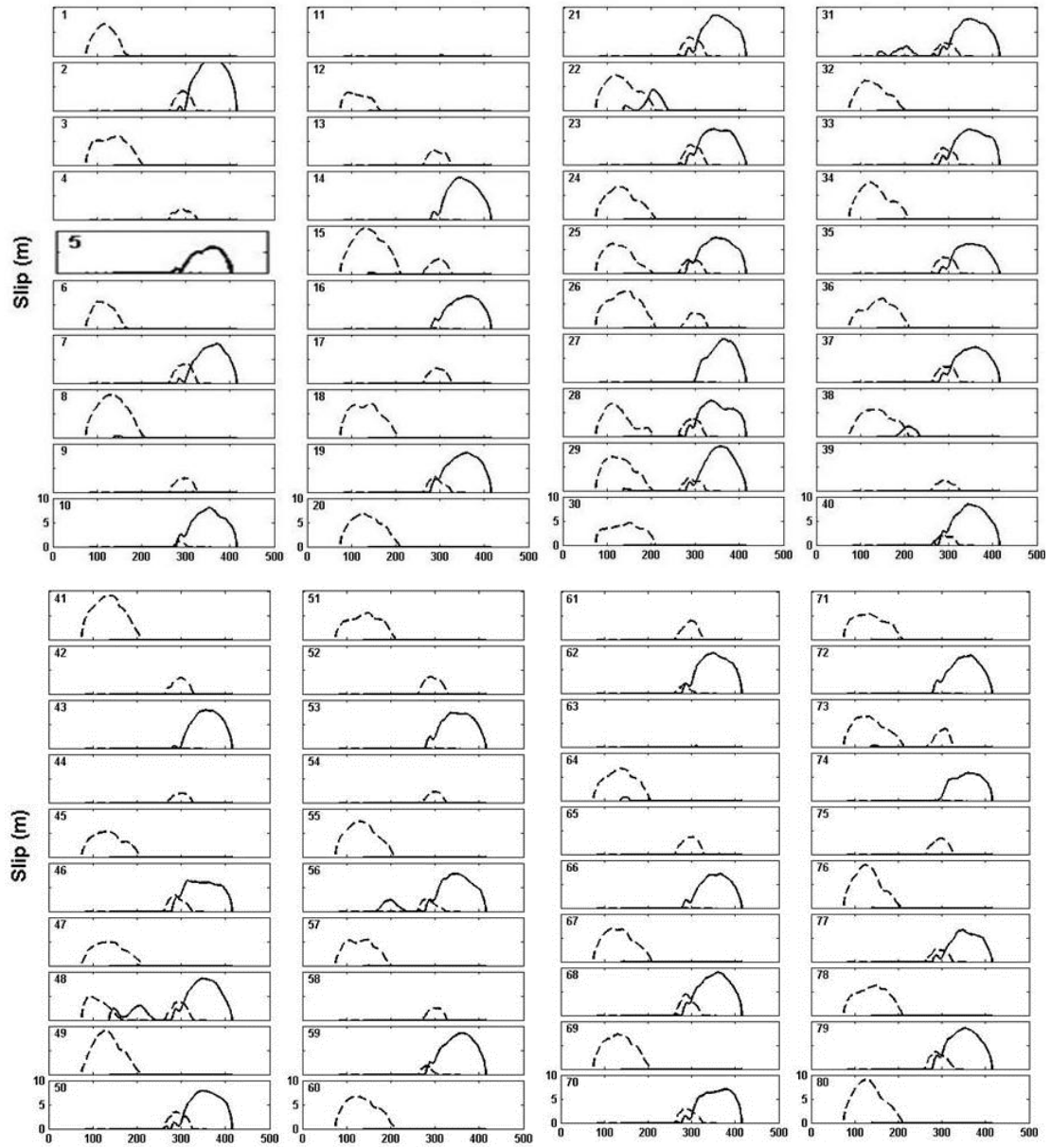
Figure 4.8 The slip distributions on the two strands of ATF in the one hundred simulated cycles.

71
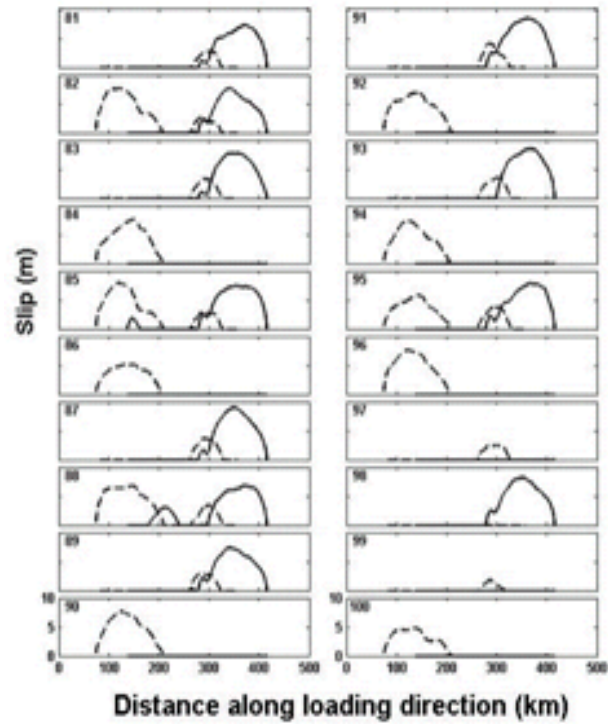
Figure 4.8 Continued

4.3.1.2 The representative events

We analyze representative events in the results of one hundred earthquake cycles in this section. We will examine the stress evolution, the accumulative slip, the slip rate evolutions and the rupturing history. Meanwhile, we will choose the cases with complex rupturing processes to discuss the possible scenarios of rupture jumping within this geometrically complex fault system.

72

One important output of our simulations is to provide possible rupturing scenarios within this geometrical complex fault system, which is unable to be pinpointed by field observations. We choose the event # 1, 5, 9, 15, 21, 22, 25, 88 as the representative events for the following discussion.

In figure 4.9, we summarize the initial stresses, final slips and the rupturing histories of those representative events. So the first rupturing scenario is that only the planar segment on the SATF ruptures just likes in the event # 1. In event # 1, we choose the center of the planar segment as the nucleation point, which could be observed at the initial stress. After propagating closely to the double-bend, it has been stopped and could no longer go into the double-bend. In event # 5, the planar segment on the NATF first nucleates, then propagates and dies at the entrance of the double-bend after propagating 25.0 second. In event # 9, nucleation occurs on the planar segment of the SATF within the double-bend, and fails to propagate out of the double-bend. In the above three scenarios, the double-bend successfully functions to either stop or trap the propagating rupture. In event # 15, the rupture nucleating on the planar segment of SATF propagates to the entrance of the double-bend. Due to the high angle between the strike and the loading direction, a certain part has been "locked", which means the yield stress is much higher than the shear stress. After 30 seconds reaching the double-bend, the rupture jumps over the "locked segment" and rejuvenates itself on the relatively planar segment within the double-bend. Here we think the double-bend prevent the rupture from jumping across the stepover and onto the NATF, even though it allows the rupture to enter the double-bend. In event # 21, the rupture nucleates at the point close to the

NATF right end; then propagates towards the double-bend. After being obstructed by the double-bend, the rupture jumps over the stepover and continues onto rupture the planar segment of SATF within the double-bend. However, the triggered rupture is unable to escape the double-bend and dies within it. In the event # 22, the rupture first nucleates roughly at the center of the planar segment of SATF, then being stopped by the double-bend. Several seconds after the rupture's nucleation on SATF, a small rupture is triggered on the left end of NATF, which is within the double-bend, but fails to grow up. After 20 seconds, the rupture continues to grow till being trapped by the double-bend again. Even though the rupture jumps over the stepover onto the other segment within the double-bend in both events # 21 and 22, it fails to jump out the double-bend. So we consider the double-bend successfully stops the rupture. In event # 25, nucleation occurs at the point close to the right end of NATF. After roughly 50 seconds, the two planar segments of SATF within and outside of the double-bend are ruptured consecutively, except the locked segment. In this scenario, we think the double-bend is only partially successful in stopping the rupture due to the failure to trap the triggered rupture within the double-bend on SATF. In event # 88, the rupture first nucleates at the point close to the left side end of SATF and propagates into the double-bend. Then the rupture jumps the stepover and triggers a rupture on the segment of NATF within the double-bend. As the moment of death of the triggered rupture on NATF within the double-bend is about to die, the planar segment of SATF within the double-bend is triggered and the rupture propagates bilaterally on that segment. Finally, the planar segment of NATF outside of the double-bend is triggered and the rupture mainly propagates away from the double

end to the fault right end. In this scenario, the double-bend has been jumped by the rupture and allows the rupture to propagate out. We consider the double-bend completely fails to serve as a barrier to the propagating rupture in this scenario. To sum up, the eight scenarios of rupturing are the possible stories, which could occur with the given fault geometry and the loading direction in our preferred model.
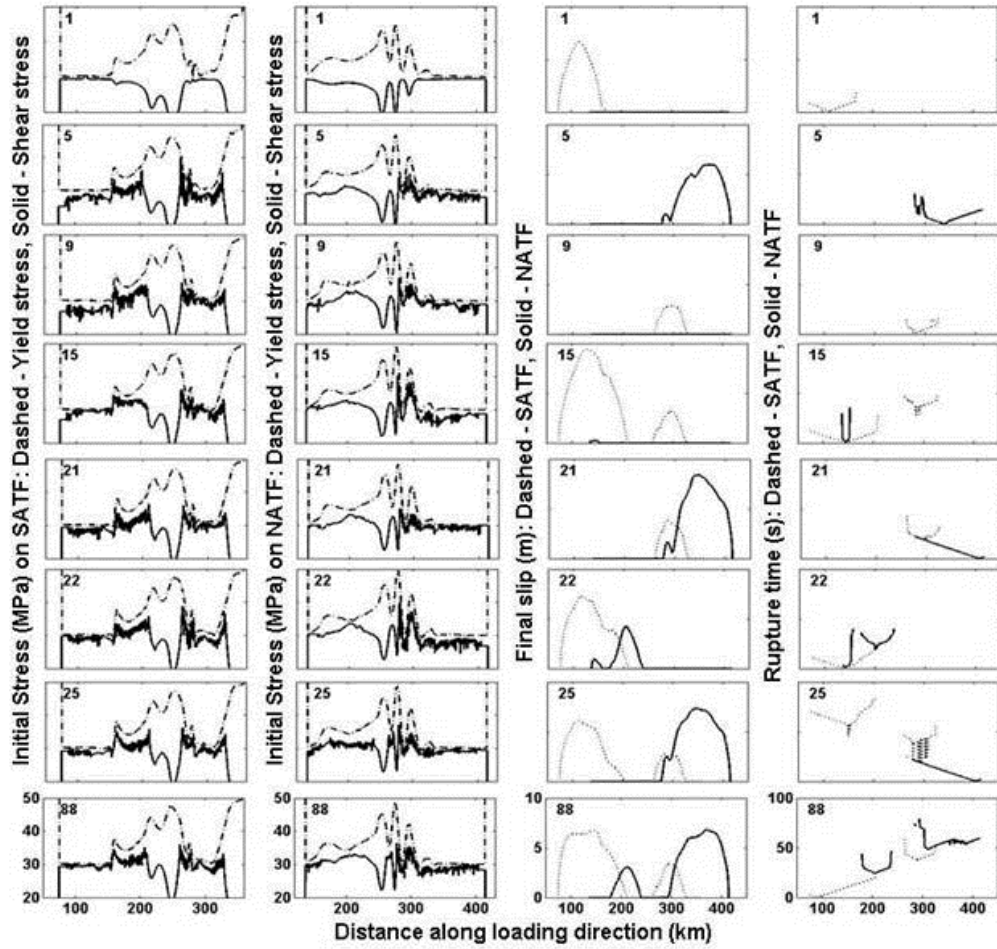
Figure 4.9 The initial stresses of the coseismic process on both strands, and the final slip distribution and the rupture time history on the representative events.

4.3.1.3 Statistic analysis of the barrier effect of the Aksay double-bend

One of the important goals of this research is to explore the effectiveness of the Aksay double-bend in stopping the seismic rupture within this complex fault geometry, which is hard to achieve by field observations. As we describe above, all the observed rupturing scenarios have been categorized into three groups: "completely stopped" by the double-bend, "partially stopped" by the double-bend and "not being stopped" by the double-bend. As shown in Figure 4.10, in our preferred model, 90% of the simulated events have been completely obstructed by the Aksay double-bend. Only 7% of the rupture has to be partially stopped by the double-bend. The rupture has 3% possibility to successfully propagate through the double-bend. So we conclude that the Aksay double-bend acts as an effective barrier to seismic ruptures either propagating towards the double-bend from outside of it or nucleating within it.
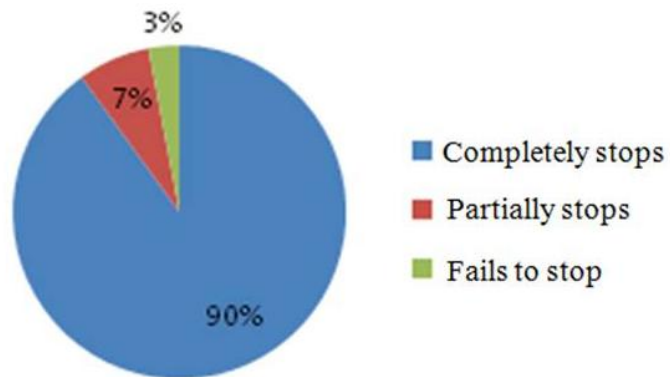
Figure 4.10 The statistic analysis of the Aksay bend's ability to work as a barrier for seismic ruptures.

The viscosity of the interseismic loading process in our model characterizes the effect of off-fault permanent deformation on the fault system (Duan and Oglesby, 2005,2006). The smaller value of viscosity means more significant off-fault permanent deformation, thus stronger effects on the fault stress. In order to test the effect of viscosity variations on the rupture behavior and the ability of double-bend to stop the rupture, we perform a group of simulations in cases with different viscosities. In the following section, we present these simulation results.

Figure 4.11 is the result of final slip of the one hundred earthquake cycles simulation with the viscosity value of $2.0 \times 10^{21}\ Pa\ S$, and all other parameters remain the same as in the preferred model. We also choose the representative events as we did in the previous case. In Figure 4.12 are the ten events, whose rupturing processes are typical and could represent all possible rupturing scenarios occurring within the one hundred earthquake cycles' simulation. The representative event numbers are: 4, 9, 11, 13, 15, 17, 18, 22, 29 and 80.

In event # 4, only the planar segment on the SATF is ruptured and then stopped by the double-bend. This kind of scenario is the most frequent one in the one hundred cycles, which accounts for 25% of the total events. As before, this rupturing scenario is defined as "completely stopped" by the double-bend. In event # 9, the rupture nucleates at a point close to the right end of NATF, and then the rupture propagates towards the double-bend. After being impeded by the double-bend, a triggered rupture on the SATF within the bend continues propagation and dies within the bend. But the rupture regains

77

nucleation on the segment of NATF within the double-bend and successfully reaches the right end of NATF. We call this rupturing scenario as "partially stopped" by the double-bend. Because the double-bend allows the rupture to rupture the entire NATF except some "locked" parts. In event # 11, the rupture first nucleates nearing the east end, and then it is stopped by the double-bend. After the rupture dies within the double-bend, the small planar segment of SATF within the double-bend is ruptured too. In this scenario, the double-bend successfully traps the triggered rupture on SATF within the bend. In event # 13, a "completely ruptured" case, the rupture first nucleates at the planar segment of NATF, outside of the double-bend. Then the planar segment of SATF within the double-bend is triggered, but fails to propagate out of the double-bend. Finally, the rupture consecutively propagates onto the segment of NATF within the double-bend and the planar segment of SATF outside. This rupturing scenario is one of the two in which we define as the "completely ruptured". In event # 15, the rupture first nucleates roughly at the center of the planar segment outside of the double-bend on SATF, and then a triggered rupture initiates on the segment of NATF within the double-bend. However, both of ruptures are stopped or trapped by the double-bend. In event #17, the rupture nucleates outside of the double-bend on the NATF and propagates bilaterally along the segment, but is completely stopped by the double-bend on west and the fault end. In event # 18, the rupture nucleates on the SATF within the bend and dies within the bend after roughly 10 seconds after the nucleation. This is another scenario in which the double-bend completely traps or stops the nucleated rupture. In event # 22, a completely ruptured event, the rupture first nucleates on the planar segment of SATF outside of the

double-bend, and then the west segment of NATF within the bend is ruptured, then the segment of SATF within the bend and finally the planar segment of NATF outside of double-bend. Event # 29 and 88 are two scenarios that the double-bend partially stops the seismic rupture. In both events, the rupture first nucleates on the planar segment of SATF outside of the double-bend, and then the west segment of NATF within the double-bend is ruptured. After that, in event # 29, the rupture chooses to continue on the planar segment of NATF; but in event # 88 the rupture jumps back to the segment of SATF within the double-bend.
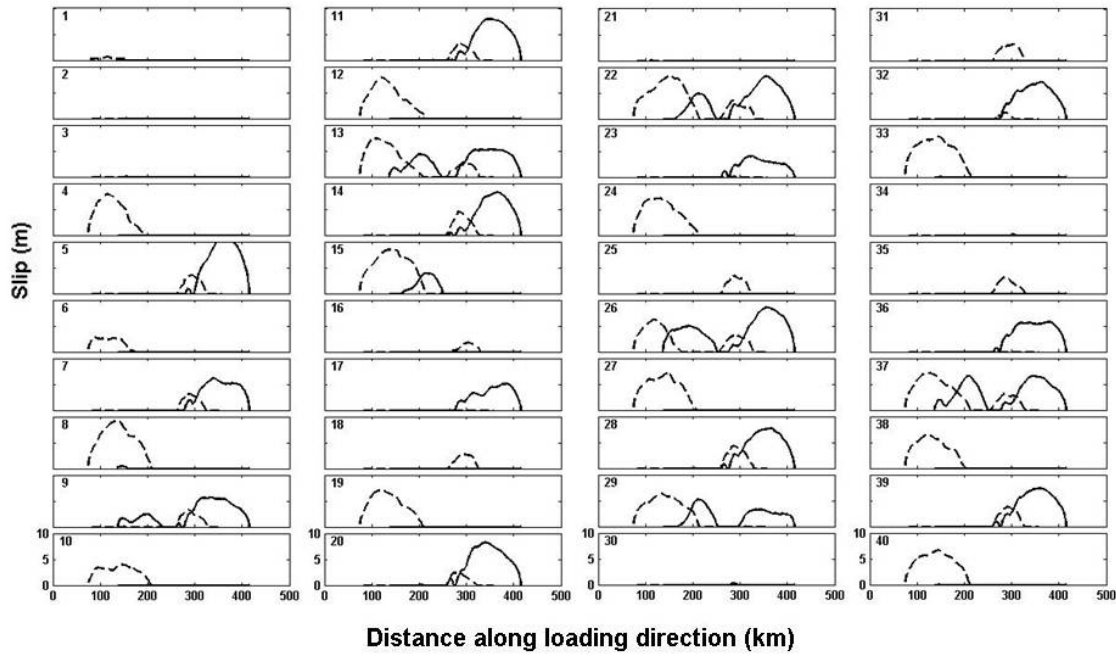
Figure 4.11 The slip distributions on the two strands of ATF in the one hundred simulated cycles in case with viscosity: $2.0 \times 10^{21} PaS$.
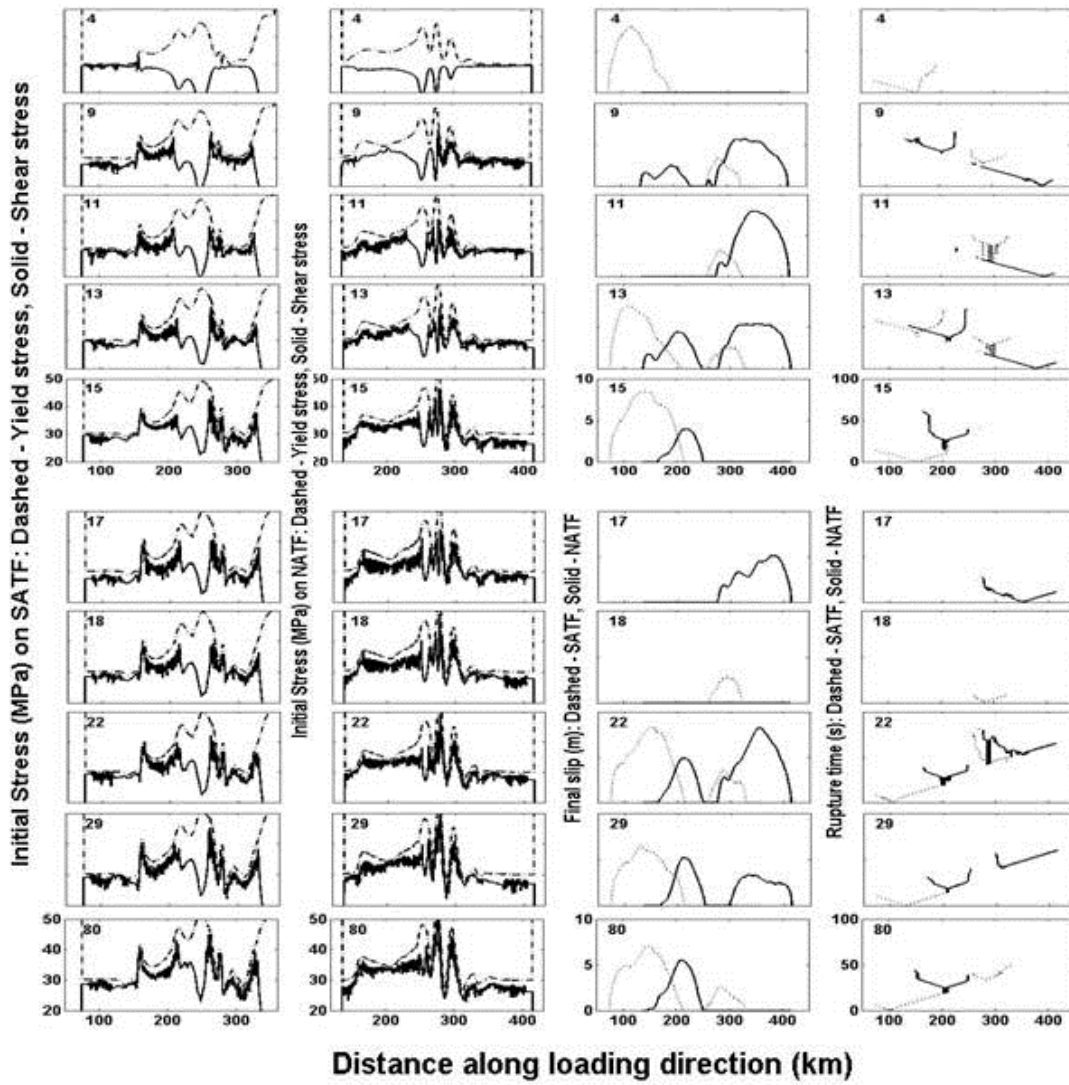
Figure 4.12 The initial stresses of the coseismic process on both of strands, the final slip distribution and the rupture time history on the representative events.

We also performed the simulations of one hundred earthquake cycles in cases with viscosities of $2.2 \times 10^{21}\ Pa\,S$ and $2.4 \times 10^{21}\ Pa\,S$, respectively. There was no exceptional rupturing scenario existing in the two cases. Therefore, we do not discuss them in details.

80

4.4 Discussion

4.4.1 The statistic analyses of the barrier effect of the double-bend

Geometrical bend and discontinuity have been regarded as the main two geometrical features to stop the seismic rupture. Several field researches have proven the effectiveness of the stepover or discontinuity in stopping the seismic rupture.

Multi-cycle simulations give us an opportunity to statistically analyze the barrier effect of the double-bend. In order to effectively categorize those results, we define three terminologies to describe the effectiveness of the double-bend in stopping the seismic rupture. We term the following scenarios as the group of "completely stop": First, the rupture nucleating outside of the bend has been stopped by the bend or the rupture nucleating inside and then is trapped within the bend. Second, if the rupture nucleates outside of the double-bend and triggers the rupture on the other strand of ATF within the double-bend, but the triggered rupture fails to escape the entrapment of the double-bend. Third, if one strand was entirely ruptured, but the rupture could not jump the stepover between NATF and SATF. We term the following rupturing scenarios as the group of "partially stop": the rupture nucleated at one strand outside of the bend and propagated into the bend, then triggered a rupture on the other strand and continued itself even outside of the bend. When the double-bend is not able to prevent the rupture from jumping the stepover and rupturing the two strands excepting the "locked segments" on both strands of ATF, we term those rupturing scenarios as the group of "fails to stop".

81
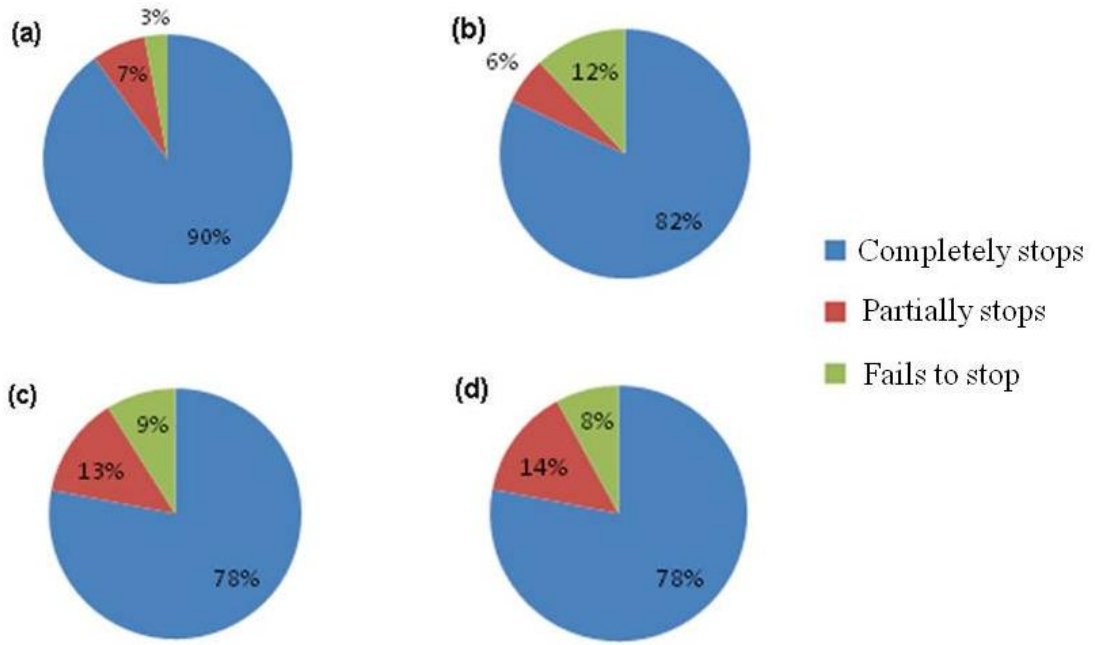
Figure 4.13 The statistic analysis of the Aksay bend's ability to stop the seismic rupture. (a) case with viscosity: $1.8 \times 10^{22} PaS$; (b) case with viscosity: $2.0 \times 10^{22} PaS$; (c) case with viscosity: $2.2 \times 10^{22} PaS$; (d) case with viscosity: $2.4 \times 10^{22} PaS$.

Figure 4.10 is the statistic analysis of the case with viscosity $= 1.8 \times 10^{21}\ Pa\ S$. It shows that 90% of the simulated events have been completely stopped by the double-bend. Only 3% of the simulated events have the chance to propagate into the double-bend, jump the stepover and finally escape out of the double-bend, which resulting in the failure of the double-bend to stop the rupture. In addition, 7% of the simulated events could only partially be stopped by the double-bend. Therefore, we conclude that the double-bend is an effective barrier to stop the seismic rupture.

Furthermore, we have done the same analysis on other cases with different viscosities in the interseismic loading process to test the consistency of double-bend in stopping the rupture under different controlling parameters. Figure 4.13 gives out the comparison of the results of the statistic analysis. We find that with the increment of viscosities, the capacity of the double-bend in completely stopping the seismic rupture has been weakened: from 90% in case with viscosity of 1.8×10^{21} Pa S to only 78 % in case with viscosity of 2.4×10^{21} Pa S. As we discussed previously, the value of viscosity represents the extent of the off-fault deformation. Therefore, our results indicate that the decreased off-fault deformation would weaken the double-bend's ability in completely stopping the seismic rupture.
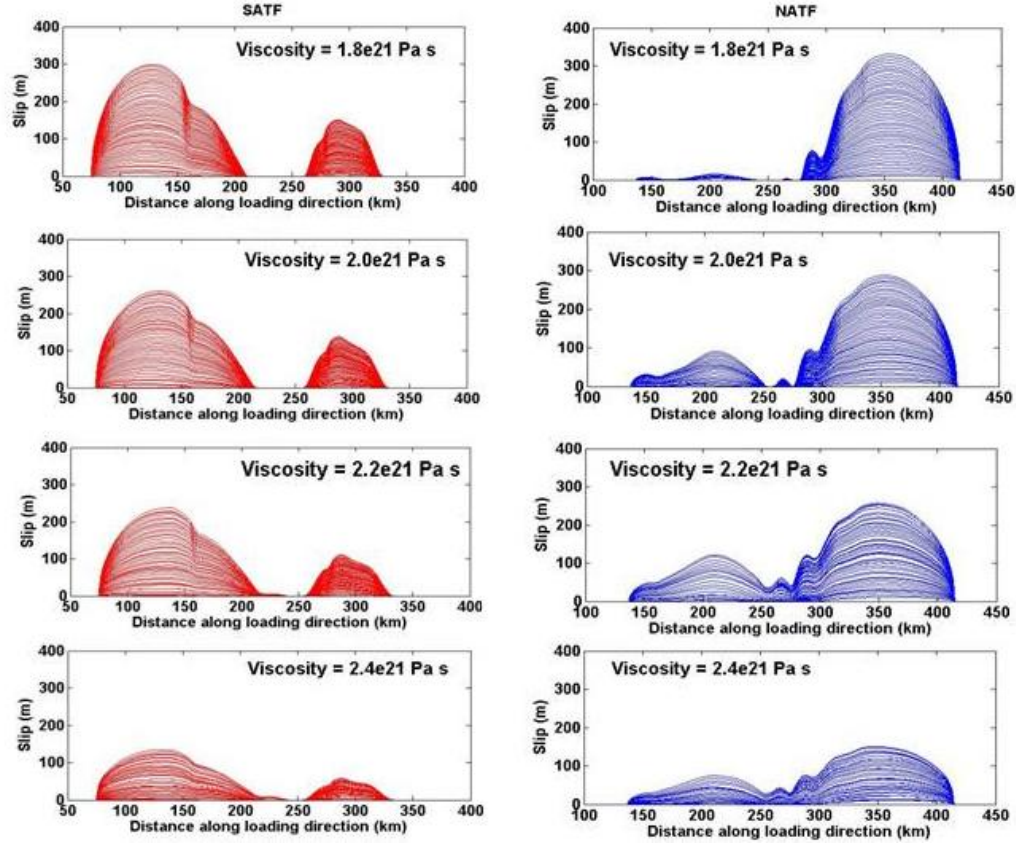
Figure 4.14 The accumulative slips of the four cases with different viscosity on both strands of ATF.

4.4.2 The accumulative slips and nucleation positions in cases with different viscosities

Other features worth discussing are the final accumulative slips and the distribution of nucleation within the one hundred earthquake cycles. We summarize the accumulative slips on both fault strands after the one hundred earthquake cycles. In figure 4.14, we observe that the final slip amount is smaller within the double-bend than

84

the slip on the segments outside of the double-bend. This could be explained by the geomorphic features inside and outside the double bend: inside of the double bend there are huge snow mountains indicating larger off-fault deformations compared with the part outside of the double bend. In addition, this can also be explained by the statistic analysis on the representative event scenarios. In many events, the rupture nucleates at the segment outside of the double-bend and then propagates bilaterally with respect to the nucleation. One side would be stopped by the fault end, and the other side would propagates into the double-bend and dies within it. The double-bend depresses the development of rupture within it. Even though, there are some events nucleating within the double-bend, but those ruptures fail to escape out of the double-bend, only resulting in a small ruptured segment. Those two rupturing scenarios accounting for roughly three quarters of the total events result in the above feature in accumulative slips: the segment outside of the double-bend has larger slip distribution than the part inside of the double-bend. Another interesting feature is that there is one part within the double-bend on SATF that has no slip. In other words, this part has been "locked". We find that it is the large angle (almost 45.0^{0}) between the loading direction and the fault strike that makes the interseismic loading mainly imposes on the normal component on that part, which results in a high shear friction strength. By comparing the accumulative final slips with different viscosities, we find that there is a trend in final slip on NATF: the slips on NATF within the double-bend become smaller and smaller with the decrement of viscosity. In other words, the increasing off-fault deformation along the ATF would

85

make the segment on NATF within the double-bend become harder and harder to be ruptured.

In addition, we also review the distribution of nucleation positions in the simulated one hundred earthquake cycles. As what we do before, we present nucleation distributions of all four cases with different viscosities in interseismic loading. In Figure 4.15, we could observe that three segments which are nearly parallel to the loading direction are the most favorable places for nucleation. This feature makes good sense, because the smaller angle between the strike and the loading direction would allows more stress to be loaded in the shear direction and less stress to be loaded on the normal direction. Even though, in this situation, the stress relaxation would be also higher in the shear direction compared with the normal direction, but the relaxed amount is much smaller than the loaded, which would make those places to be unfavorable by the nucleation. Furthermore, we could find that the nucleation can occurs along a longer segment within the bend of NATF with a larger viscosity. We attribute this feature to the stress heterogeneity developing during the multi-cycle simulations. Larger viscosity results in stronger stress heterogeneity. Therefore, the first order features of nucleation distribution are controlled by the angle between the strike and loading direction, and secondary features are controlled by the stress heterogeneity developed over multiple earthquake cycles in the models.
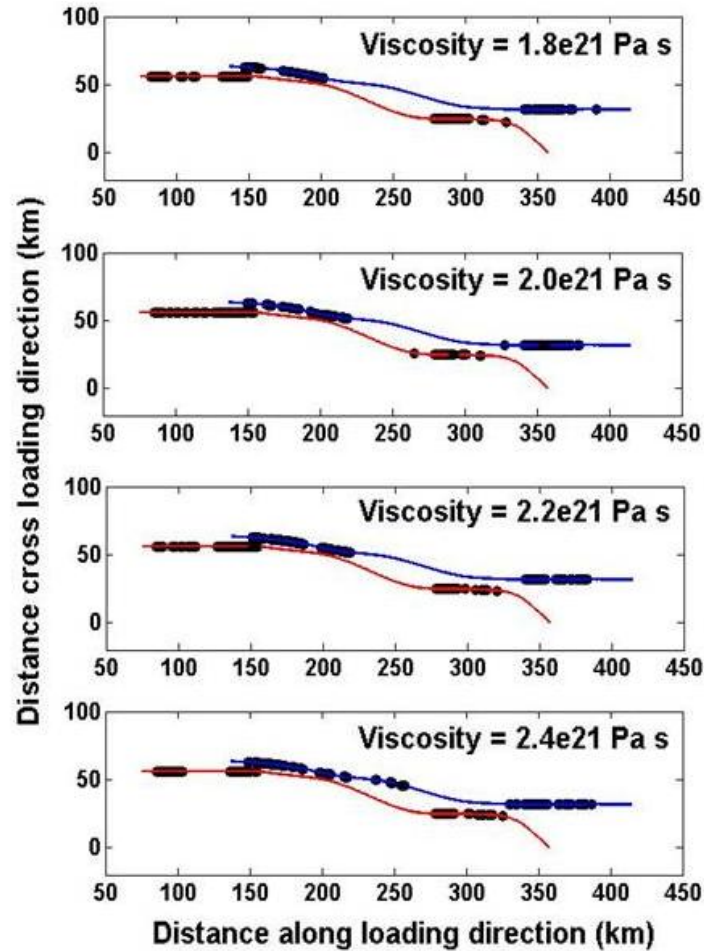
Figure 4.15 The distribution of nucleation positions of the one hundred simulated events in the four cases with different viscosities.

4.4.3 The effects of smaller stress drop: an increased dynamic friction coefficient

The field measured seismic slips (Xu,et al., 2009; Ponti, 1993; Sieh et al., 1993) put

constraints on our choices of the value of dynamic friction coefficient. Under the present

friction law we are using, the slip and rate dependent friction law, the smallest dynamic

friction coefficient that can be used is 0.5. Here now, we simulate a case with a larger

dynamic friction coefficient: 0.55, but with all the same other parameters as the preferred

model. We want to know to what extent the above conclusions would be altered by the

case with a larger dynamic friction coefficient (thus a smaller stress drop).
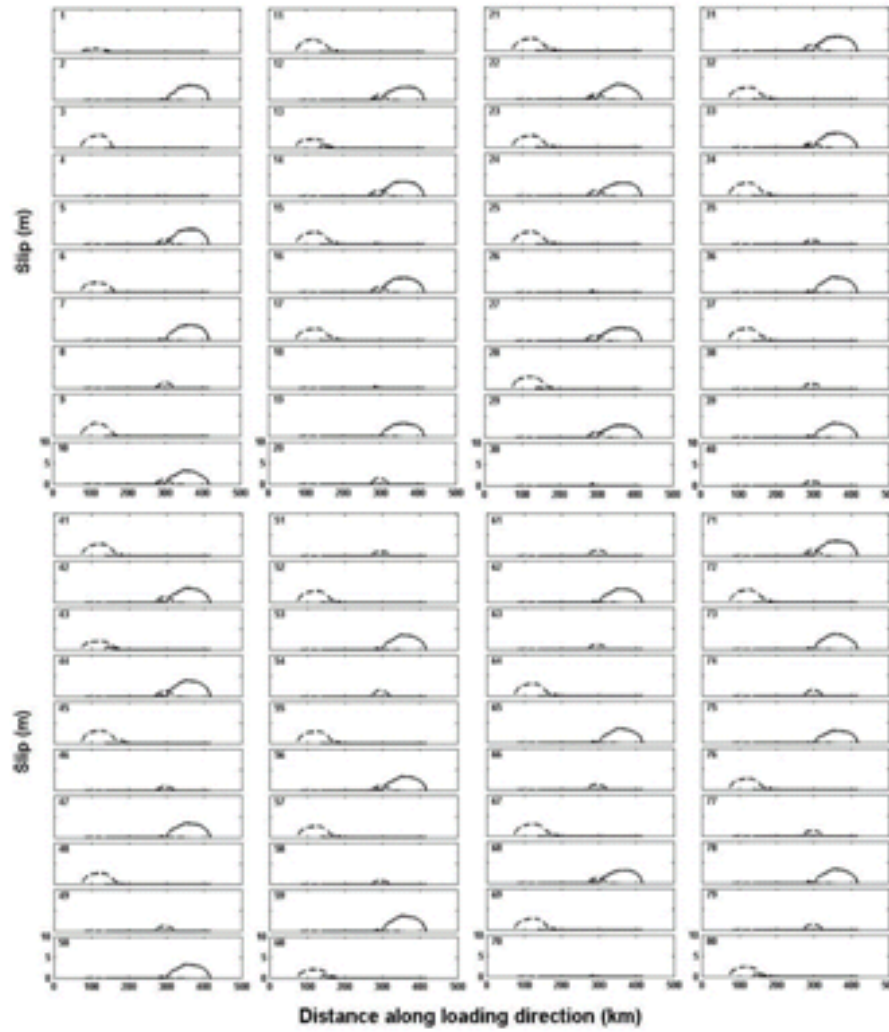
Figure 4.16 The slip distributions on the two strands of ATF in the one hundred simulated cycles in case with the dynamic friction coefficient 0.55.
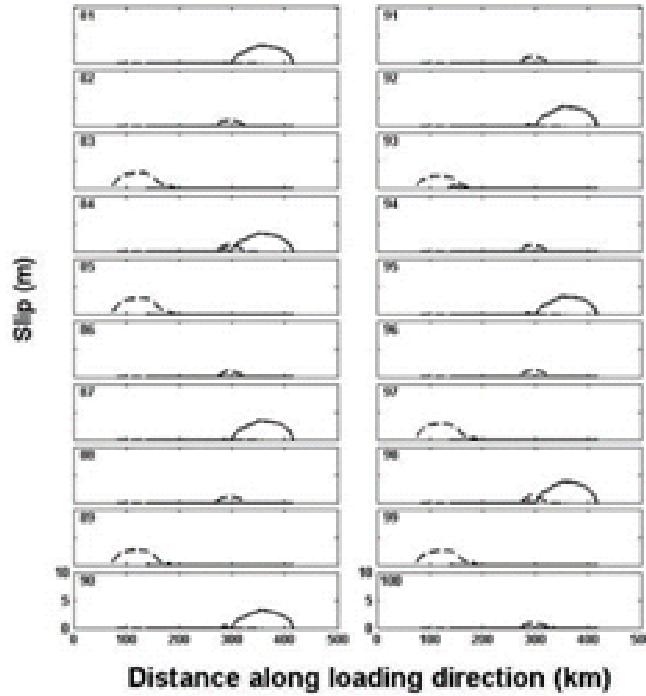
Figure 4.16 continued

Figure 4.16 gives out the final slip distribution of the simulated one hundred earthquake cycles. We observe that the maximum slips in this case are generally smaller than that in the main case. We calculate the stress drops of event # 15 in both the main case and this case. In figure 4.17, the main case, which is with a smaller dynamic friction coefficient: 0.5, has a larger stress drop on the ruptured segment compared with the case with larger dynamic friction coefficient: 0.55. We know that the average seismic slip is proportional to the average stress drop on the ruptured segment. So it is expected to have a smaller average slip in the case with a larger dynamic friction coefficient (thus a smaller stress drop).

89
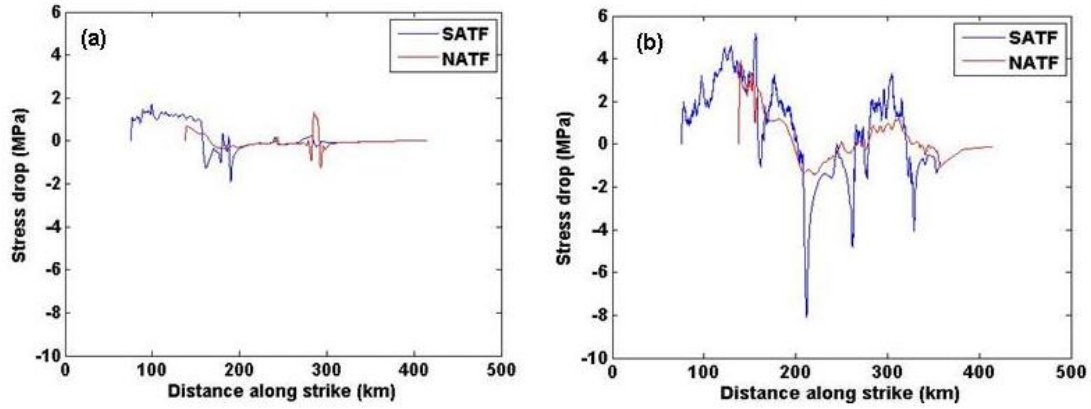
Figure 4.17 The stress drops in event # 15. (a) case with dynamic coefficient 0.55; (b) case with dynamic coefficient 0.50. Positive values are on the ruptured.

In Figure 4.18, we choose the representative rupturing scenarios in the simulated one hundred cycles. There are only four identified representative rupturing scenarios within the one hundred cycles. In event # 3, only the planar segment on SATF outside of the double-bend is ruptured, and then it is completely stopped by the double-bend. In event # 5, the rupture nucleates at roughly the center of the planar segment of NATF, which is outside of the double-bend. After rupturing the entire planar segment and being stopped by the double-bend, the rupture jumps the step and triggers a small portion of the segment on SATF within the double-bend. In event # 7, only the planar segment on NATF outside of the double-bend is ruptured, and the double-bend successfully stops the rupture. In event # 8, only the small planar portion inside of the double-bend on the SATF is ruptured, and the rupture dies within the double-bend.

90
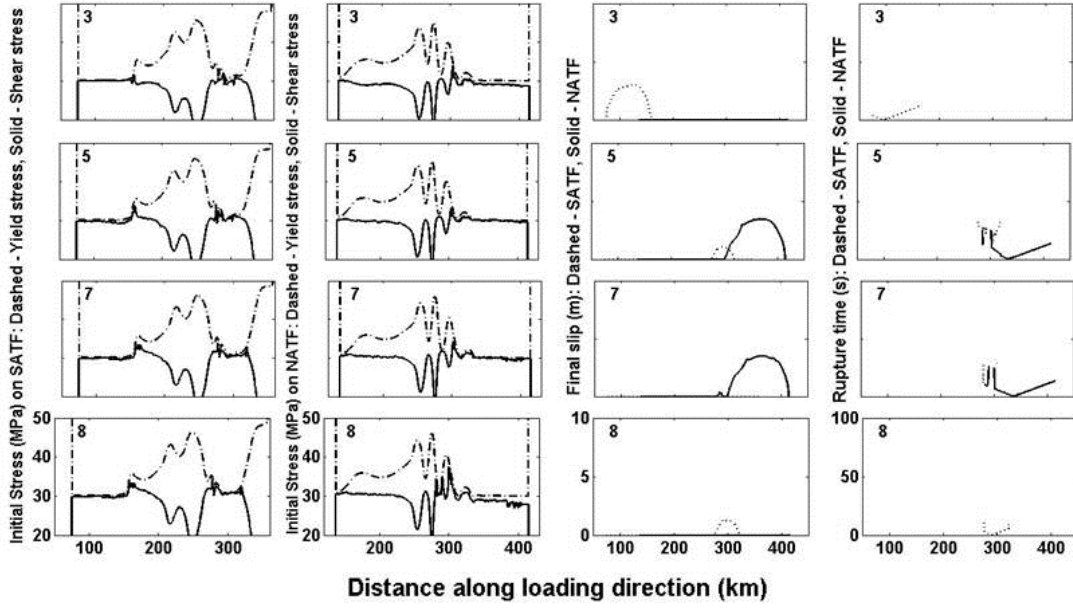
Figure 4.18 The initial stresses of the coseismic process on both of strands, the final slip distribution and the rupture time history on the representative events.

Compared with the main case and other cases with a lower dynamic friction coefficient 0.50, the diversity of rupturing scenarios has been weakened. The higher dynamic friction coefficient reduces the average stress drop on the ruptured segment resulting in a decreased seismic energy budget and a slower rupture velocity.

4.4.4 Slip-weakening law versus slip-and-rate weakening law

Here we discuss the effect of using different friction law on the simulation results. In our code, we have both of slip weakening law and slip and rate weakening law available. So in the following discussion, we will first introduce the difference between the two

91

friction laws, and then we will focus on the comparison of results employing the two different friction laws.

4.4.4.1 Comparison of slip-weakening law and slip-and-rate weakening law

Slip-weakening law was theoretically introduced by Ida (1972) and Palmar and Rice (1973), in which they consider the friction is weakened by the increment of slip within a critical distance D_c. It is simple and easy to be coded, so it has been wildly used in the past several decades in rupture modeling community. In addition, there are other researches using modified slip weakening friction law, for example, including a slip hardening phase and an exponential decrease of traction with displacement (Ohnaka, 1996). Dietrerich (1979, 1984) and Ruina (1980, 1983) proposed the variation of traction on frictional surface is the function of slip rate and the state of the frictional surface, and the rate and state friction law has become more and more popular in the rupture modeling field now. Here in our code, we do not have the standard rate and state friction law in place. Therefore, we choose to use a modified blender of the slip weakening law and the rate weakening law in our simulation, which is originally proposed by Aagard (1999).
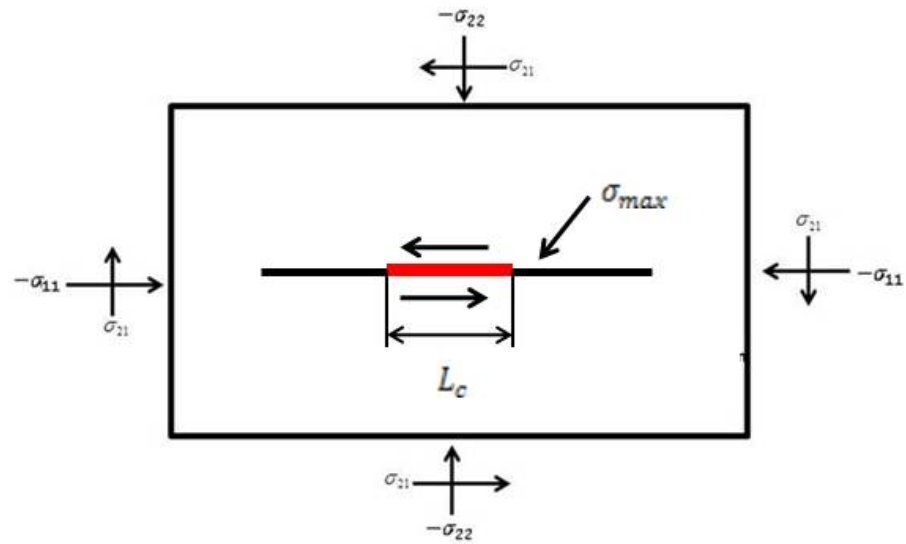
Figure 4. 19 The model geometry for the comparison of slip weakening friction law and the slip and rate friction law. The red line is the size of the nucleation patch.
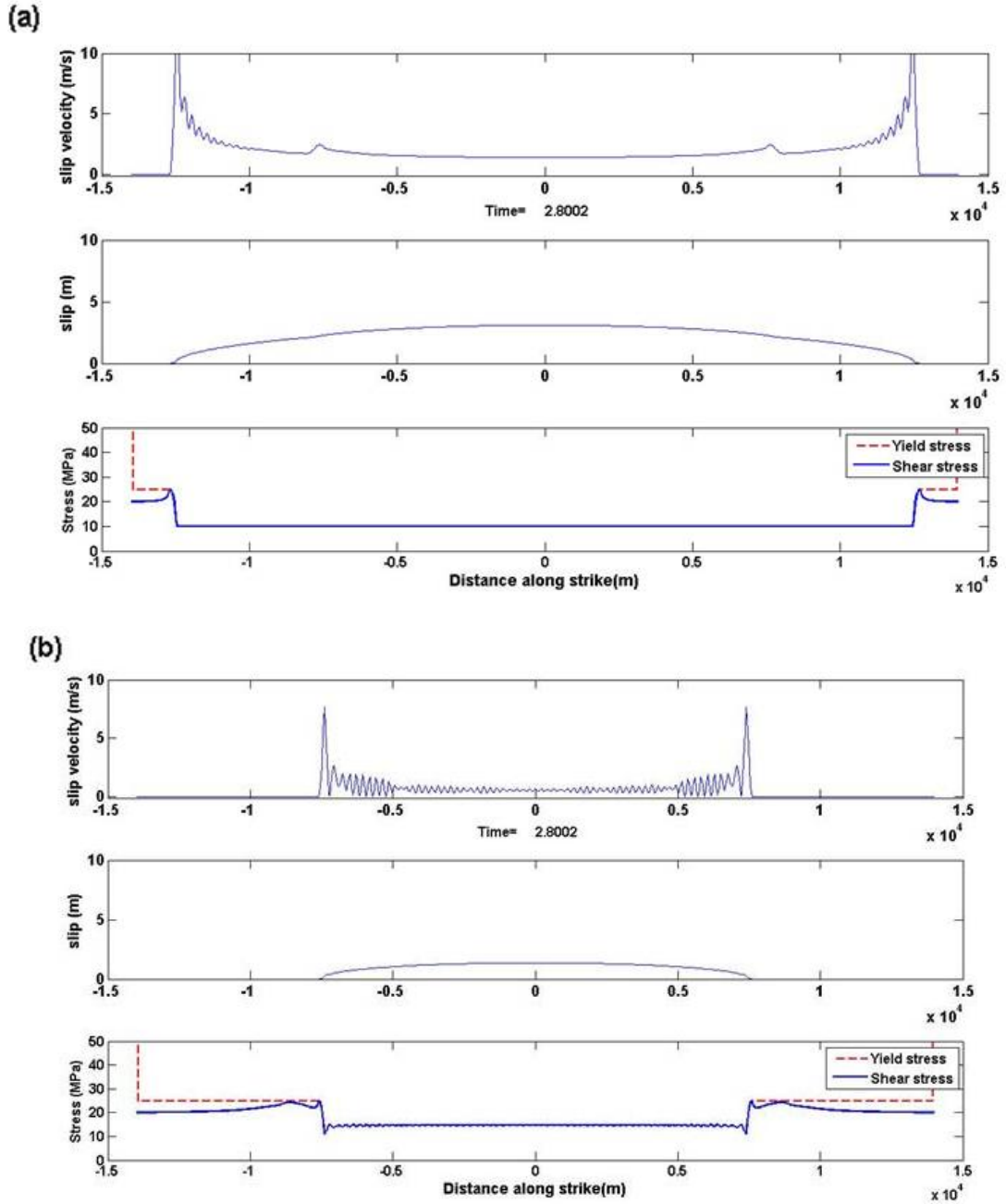
Figure 4. 20 Snapshot of slip velocity, slip and stresses on the strike-slip fault after the rupture propagates 2.8 seconds. (a) case with slip weakening friction law; (b) case with slip and rate weakening friction law with critical velocity: 10.0 m/s; (c) case with slip and rate weakening friction law with critical velocity: 20.0 m/s.

(c)
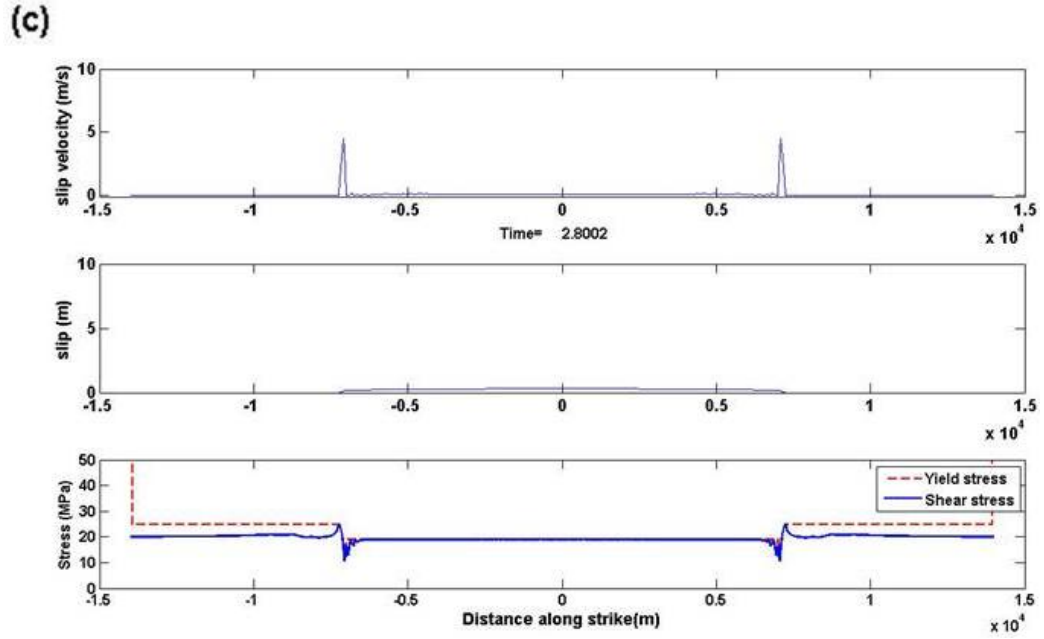
Figure 4.20 Continued.

In the following paragraph, we discuss the general differences between the slip-weakening law and the slip-and-rate weakening law in a simplified planar strike-slip fault (Figure 4.19). We use the same simulation parameters in the two cases with slip-weakening law and slip-and-rate weakening friction law respectively, except that in the

slip-and-rate weakening friction law we need to assign a healing value ($\mu_{healing} = 0.45$)

to the dynamic friction and a critical velocity ($v_{critical} = 10.0 \ ^m/_s \ and \ 20.0 \ ^m/_s$).

Figure 4.20 gives out the comparison of the three cases: $\boldsymbol{a}$ is the case with slip-weakening law; $\boldsymbol{b}$ and $\boldsymbol{c}$ are cases with slip-and-rate weakening law, but with different critical velocity values ($10.0 \ ^m/_s \ and \ 20.0 \ ^m/_s$). It is obvious that, even under the same frictional parameters ($u_d \ and \ u_s$) and same initial stresses ($\sigma_\tau \ and \ \sigma_n$), the slip-weakening law and the slip-and-rate law would generate significantly differences in the evolution of slip velocity, accumulative slip and the stresses during the dynamically rupturing process. One of the important differences among those cases is the rupture type: in case $\boldsymbol{a}$ with slip weakening law, the rupture is a crack-like rupture, which means that the node on the fault surface is still moving even after the rupture front passes across in case, $\boldsymbol{c}$ with slip-and-rate weakening law, but with the critical velocity = 20.0 m/s, the rupture is a pulse-like rupture, which means the node on the fault surface is no longer in motion after the passage of the rupture front, in case $\boldsymbol{b}$ also with slip-and-rate weakening law, but with the critical velocity = 10.0 m/s, the rupture is a hybrid of $\boldsymbol{a}$ and $\boldsymbol{c}$, in which the node on fault surface is not totally motionless after the passage of rupture front, but with a much smaller velocity compared with the nodes in case $\boldsymbol{a}$. Furthermore, we could find that the rupture in case with slip-weakening law propagates faster and have a larger final slip than the rupture in cases with slip-and-rate law under the same frictional parameters (($u_d \ and \ u_s$) and same initial stresses ($\sigma_\tau \ and \ \sigma_n$). In addition, within the two cases with slip-and rate friction law, the case $\boldsymbol{b}$ has a larger final slip distribution

96

than the case c due to the smaller critical velocity. The stress drop distributions (not shown) of the three cases are consistent with the final distributions: the larger stress drop results in a larger final slip.
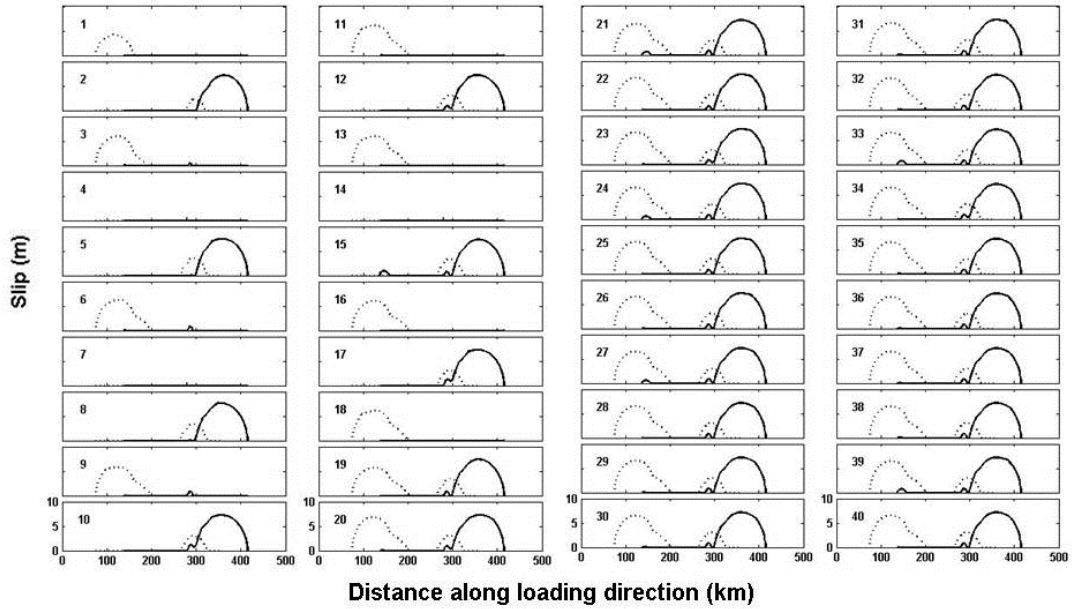
Figure 4.21 The slip distribution of the first forty events of the case with slip weakening law.

4.4.4.2 The simulation results with slip-weakening law

In this part, we present the simulation results from the case by using slip weakening friction law with $\mu_d = 0.57$ and $\mu_s = 0.60$. In the early stage of this project, we first employ the traditional slip weakening friction law. It is our first attempt to use the slip

weakening law in this kind of complex fault geometry with the multicycle simulator. So we encountered several challenges, which force us to turn to the slip and rate friction law. In the following discussion, we will first present the results with slip weakening friction law, and then discuss those problems in the results.

Figure 4.21 is the final slip distribution in the first 40 events. One can see that all the events after event # 20 keep having the same slip distribution pattern: on SATF the entire fault is ruptured except the "locked" segment and on NATF only the planar segment outside of the double-bend is ruptured. It means that the system reaches the "stable status" after the event # 20. Stable status means the evolution of stresses has reached stable situation, and it remains in the same status even with the process of multi-cycle simulation. The swiftness of reaching stable status is not a good sign for our multi-cycle simulations: it is not the way occurring in nature. The most important factor contributing to the swift form of stable status is the relatively small difference between the static and dynamic frictional coefficients. After several cycles, those planar segments would become more and more synchronized either on the interseismic loading process and the seismic process. The steady state occurs due to the simplified fault system. In our model now, we have a very long fault system which makes 2D models depart from what is occurring in nature. The 2D fault model artificially removes the healing signal rebounding from the seismogenic depth. The quickest way which we think has the potential to resolve this problem is the involvement of the slip rate into the friction law. Many previous researches pointed out that the involvement of slip rate into friction law

would make the residual stresses after a seismic rupturing become heterogeneous, which we think could avoid the quick appearance of the steady status in stress distribution.

4.4.5 The length of interseismic loading and slip rate

We record the time length of each interseismic loading process. The time length of interseismic loading could be one of the several simulated results which we could use to compare with paleoseismic researches to evaluate the quality of our simulated results.

Figure 4.22 gives out the distribution of time length of the interseismic loading in the one hundred earthquake cycles simulations. In this figure, we summarize cases with different viscosities. Just like what we expect that the case with lowest viscosity: $1.8 \times 10^{21} Pa\, s$ has the largest average interseismic loading time. And the case with largest viscosity: $2.4 \times 10^{21} Pa\, s$ has the shortest average interseismic loading time. The larger viscosity means less off-fault relaxation resulting in shorter loading time before the shear stress reaches the shear strength on the fault. On contrary, the smaller viscosity means larger off-fault relaxation which could enlarge the time needed by the shear stress to reach the shear strength. This could also be observed in the number of events with different interseismic loading time. In the case with viscosity: $1.8 \times 10^{21} Pa\, s$, the number of events with interseismic period more than 1000 years is much more than the other three cases. With the increase of viscosity value, the events with smaller interseismic period (< 200 years) become more frequent. Washbum et. al. (2001) carried out paleoseismic research on the central Altyn Tagh fault and two paleoseismic events have been identified. The possible recurrence intervals of the two paleoseismic events are: 0.7 ± 0.4 k.y. and 1.1 ± 0.3 k.y., respectively. The recurrence intervals (or

time length of the interseismic loading) in our results are comparable with the two field-measured values: in case with viscosity:$1.8 \times 10^{21} Pa\ s$, the largest recurrence interval is 1.520 k.y. and recurrence of interval 0.3 k.y. is a common value in our simulation results.
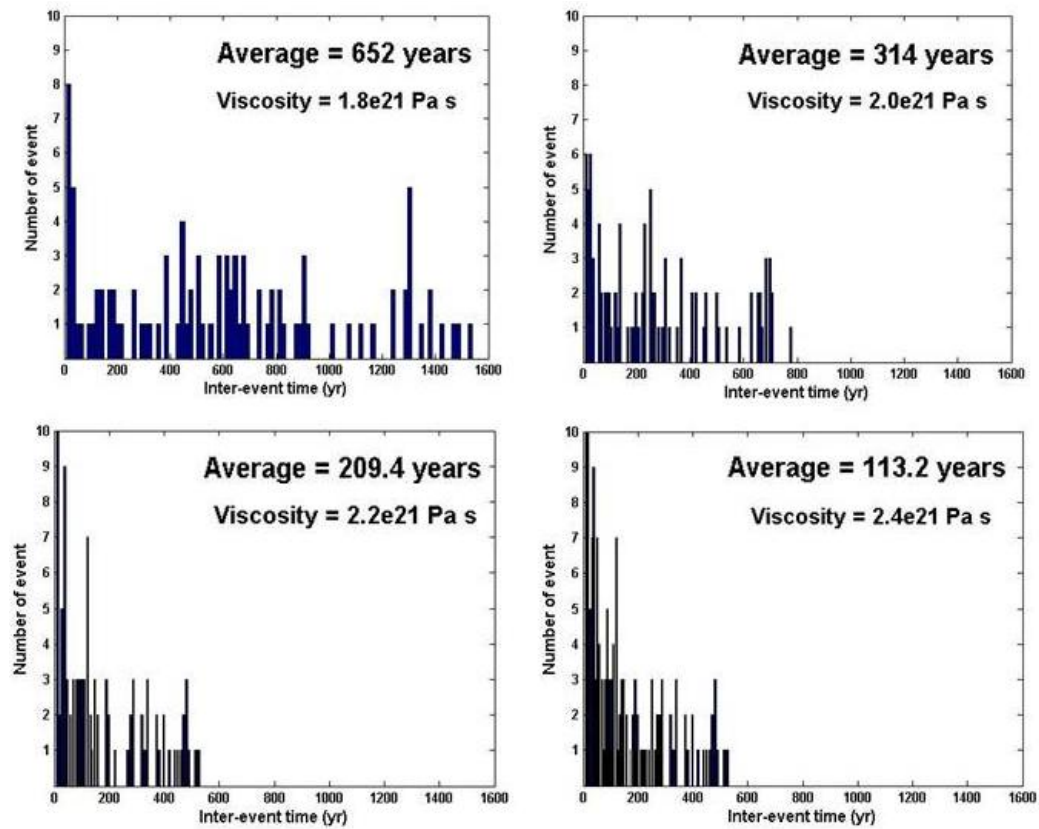

Figure 4.22 The analysis of interseismic loading time in four cases.

Paleoseismologists usually use the geomorphological features to derive the seismic offsets in paleoseismic events, and date the events by using stratigraphic features. So the

slip rate on certain fault segment is one of the typical outputs of paleoseismic researches. There are several paleoseismic slip-rate researches existing on the Altyn Tagh fault, and our collaborators are also conducting a more detailed paleoseismic research focusing on the segment of Aksay bend of the ATF. Those researches provide us an opportunity to compare the slip-rate calculated from simulated results to the field-researched slip-rate. Figure 4.23 is the summary of the slip-rate along the center segment of Altyn Tagh fault. It is obvious that the slip-rate at a specific location may have different values estimated by using different methods. But generally, we could observe that at, the vicinity of Aksay bend (the yellowed region), the real measured slip-rate value is within the range of 5 ~ 25 mm/yr. In our model, we have recorded the time length of the interseismic process. In further, we have the final accumulative slip along the fault. So we could calculate the final slip rate distribution along the fault and compare it to the filed-measured slip rate, which could help us evaluate the quality of our simulation results. We are not attempting to compare the value of the simulated slip rate with the field-measured slip rate at specific locations on the fault. We want to make sure that our simulated slip rate is roughly comparable with the field-measured ones. In figure 4.24, we present the simulated slip rate in the all the four cases with different viscosities. We could find that in the four cases the maximum values of slip rate are within the range of field-measured values. And the maximum values are proportional to the viscosities used in the model.

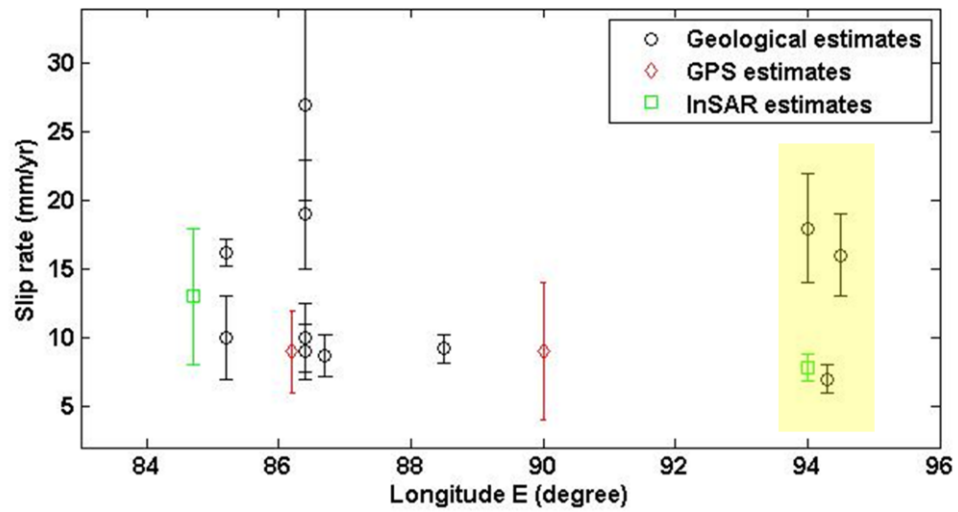**Figure 4.23 The estimates of slip rate along the Altyn Tagh fault by using different methods modified from He et al., (2013).**
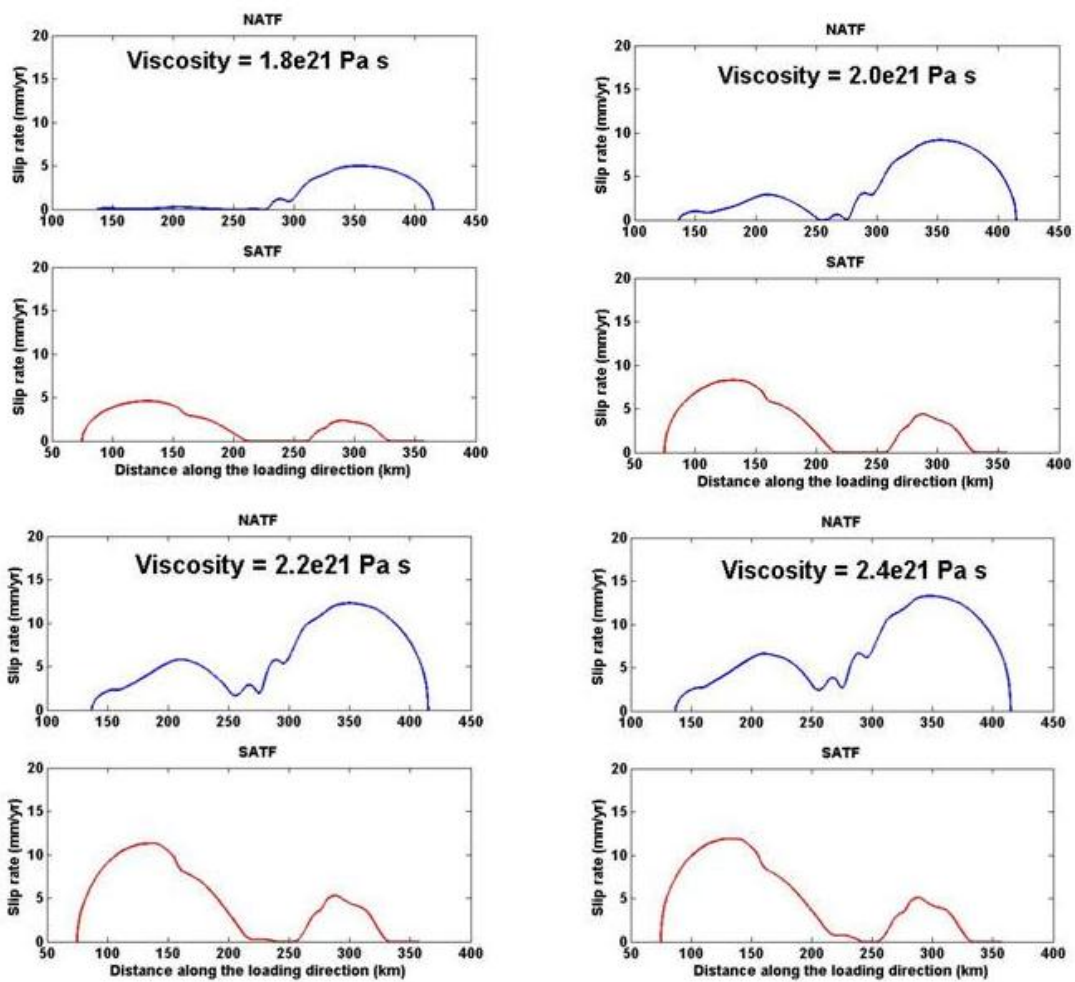
Figure 4.24 The final slip rate distributions along the two strands of the Altyn Tagh fault near the Aksay bend.

5. CONCLUSION

Effects of off-fault damage and pore pressure changes at a stepover on rupture dynamics of parallel strike-slip faults are examined using spontaneous rupture models. We find that the distribution and evolution of the positive Coulomb stress (PCS) determine whether or not a propagating rupture on the first fault of a stepover can jump across a stepover onto the second fault, and the location and time of rupture initiation on the second fault if rupture jumps. A split crescent-shaped PCS patch propagating away from the end of the first fault controls rupture initiation on the second fault in the compressive stepover, while a PCS lobe that gradually grows from the end of the first fault dominates rupture jumping behavior in the dilatational stepover. Off-fault damage in the form of plastic yielding allows a propagating rupture to jump across a dilatational stepover in which the two fault segments are barely overlapped, while a certain amount of overlap is required for the rupture to jump in the absence of off-fault damage. The maximum jumpable width for a dilatational stepover can be significantly reduced by time-dependent pore pressure. When both time-dependent pore pressure and off-fault damage are present, the former dominates rupture jumping behavior at a stepover.

We verify the linear relationship between near-tip slip gradient near the stepover and the capacity of the rupture to jump on a fault with a fixed length, which is an add to the threshold of slip gradient proposed by Elliot et al.(2009). In addition, the physical mechanism behind is the stress distribution, which could control the slip gradient and the rupture's jumping ability. Furthermore, the slip gradient over the last 1 km is the indicator of the average stress drop on the entire first fault during the coseismic process.

104

Right now, we only discuss the slip gradient effect in the elastic model, and this topic is also worth further researching in model with off-fault plasticity in future.

In our model configuration in section 4, the relatively planar segments outside of the double-bend on both SATF and NATF have been favored by the loading direction to be ruptured due to their strikes roughly parallel to the loading direction. One segment on SATF is "locked" in the simulations, because its strike has a large angle ($\sim45.0^{0}$) with respect to the loading direction. Multiple rupturing scenarios have been observed in the simulation results implying the interaction between the two strands of ATF through the Aksay bend (the double-bend). The statistic analysis indicates that the double-bend effectively keeps the seismic rupture either from entering the double-bend if the rupture nucleates outside of the double-bend or escaping the double-bend if the rupture nucleates inside it in almost 90 percent of the simulated events. In 3% of the simulated events, the double-bend fails to stop or trap the seismic rupture nucleating outside or inside of it. In 5% of the simulated events, the seismic rupture is partially stopped by the double-bend. So we conclude the double-bend is an effective barrier for the seismic rupture under the current model configuration. Viscosity in our model represents the extent of off-fault deformation. Our results indicate that the effectiveness of the double-bend in stopping the rupture is affected by the extent of off-fault deformation we assign in the model: the larger off-fault deformation would make the double-bend more effective in functioning like a barrier for the seismic rupture.

105

REFERENCES

Allmann, B. P., and P. M. Shearer (2009), Global variations of stress drop for moderate to large earthquakes, J. Geophys. Res., 114, B01310, doi: 10.1029/2008JB005821

Andrews, D.J. (2005), Rupture dynamics with energy loss outside the slip zone, J. Geophys. Res., 110, B01307, doi: 1029/2004JB003191

Andrews, D. J. (1976), Rupture velocity of plane strain shear cracks, J. Geophys. Res., 81, 5679-5687.

Andrews, D. J. (1985), Dynamic plane-strain shear rupture with a slip-weakening friction law calculated by a boundary integral method, Bull. Seismol. Soc. Am., 75, 1-21.

Aochi, H., E. Fukuyama, and M. Matsuura (2000), Selectivity of spontaneous rupture propagation on a branched fault, Geophys. Res. Lett., 27(22), 635-638.

Ben-Zion, Y., and Z. Shi (2005), Dynamic rupture on a material interface with spontaneous generation of plastic strain in the bulk, Earth Planet. Sci. Lett., 235, 486-496, doi: 10,1016/j.epsl.2005.03.025.

Bernard, P., and R. Madaraiga (1984). A new asymptotic method for the modeling of near-field accelerograms, Bull. Seismol. Soc. Am. 74, 539-558

Burchfiel, B.C., and J.H.Stewart (1966), "Pull-apart" origin of the central segment of Death Valley, California, Geol. Soc. Am. Bull., 77, 439-442

Byerlee, J.D. (1978), Friction of rocks, Pure Appl. Geophys., 116, 615-626

Chester, F.M., J.P.Evans, and R.L.Biegel (1993), Internal structure and weakening mechanisms of the San Andreas fault, J. Geophys. Res., 98, 771-786.

Cochard, A., and Madariage, R. (1994), Dynamic faulting under rate-dependent friction, PAGEOPH, 142, 419-445

Day, S. M. (1982), Three-dimensional simulation of spontaneous rupture: The effect of nonuniform prestress, Bull. Seismol. Soc. Am, 72, 1881-1902

DeDontney, N., J.R.Rice, and R. Dmowska (2011), Influence of material contrast on fault branching behavior, Geophys. Res. Lett., 38, L14305, doi: 10.1029/2011GL047849

Duan, B., and D. D. Oglesby (2006), Heterogeneous fault stresses from previous earthquakes and the effect on dynamics of parallel strike-slip faults, *J. Geophys. Res.*, 111, B05309, doi:10.1029/2005JB004138.

Duan, B., and S.M.Day (2008), Inelastic strain distribution and seismic radiation from rupture of a fault kink, J. Geophys. Res., 113, B12311, doi: 10.1029/2008JB005847

Duan, B. (2008b), Asymmetric off-fault damage generated by bilateral ruptures along a biomaterial interface, Geophys. Res. Lett., 35, L14306, doi: 10.1029/2008GL034797

Duan, B. (2008a), Effects of low-velocity fault zones on dynamic ruptures with nonelastic off-fault response, Geophys. Res. Lett., 35, L04307, doi: 10.1029/2008GL033171

Duan, B., and S. Day (2010), Sensitivity study of physical limits on ground motion at Yucca Mountain, *Bull. Seismol. Soc. Am.*, 100 (6), 2996-3019, doi:10.1785/0120090372.

Elliott, A.J., J.F.Dolan, and D.D.Oglesby (2009), Evidence from coseismic slip gradients for dynamic control on rupture propagation and arrest through stepovers, J. Geophys. Res., 114, B02312, doi: 10.1029/2008JB005969

Finzi, Y., and S. Langer (2012), Damage in step-overs may enable large cascading earthquakes, Geophys. Res. Lett., 39, L16303, doi: 10.1029/2012GL052436

Harris, R. A., R. J. Archuleta, and S. M. Day (1991), Fault steps and the dynamic rupture process: 2-d numerical simulations of a spontaneously propagation shear fracture, Geophys. Res. Lett., 18, 893-896

Harris, R., M. Barall, D. J. Andrews, B. Duan, S. Ma, E.M.Dunham, A. −A. Gabriel, Y. Kaneko, Y. Kase, B.T. Aagaard, D.D.Oglesbym, J.-P. Ampuero, T.C.Hanks, and N. Abrahamson (2011), Verifying a computational method for predicting extreme ground motion, Seismol. Res. Lett., Vol. 82, No. 5, 638-644, doi:10.1785/gssrl.85.5.638.

Harris, R.A., M.Barall, R.Archuleta, E.Dunham, B.Aagaard, J.P.Ampuero, H.Bhat, V. Cruz-Atienza, L.Dalguer, P.Dawson, S.Day, B.Duan, G.Ely, Y.Kaneko, Y.Kase, N.Lapusta, Y.Liu, S.Ma, D.Oglesby, K.Olsen, A.Pitarka, S.Song, and E.Templeton (2009), The SCEC/USGS dynamic earthquake-rupture code verification exercise, Seismol. Res. Lett., vol. 80, No.1, 119-126, doi: 10.1785/gssrl.80.1.119

Harris R. A. and Day S. M. (1993), Dynamics of fault interaction: parallel strike-slip faults, J. Geophys. Res. 98, 4461-4472

Ida, Y. (1972), Cohesive force across tip of a longitudinal-shear crack and Griffiths specific surface-energy, J. Geophys. Res., 77, 3796-3805.

Kanamori, H., H.-K. Thio, D. Dreger, E. Hauksson and T. Heaton (1992), Initial investigation of the Landers, California. Earthquake of 28 June 1992 using TERRAscope, Geophys. Res. Lett. 19, 2267-2270

Liu, Z. and Duan B. (2014), Dynamics of parallel strike-slip faults with pore fluid pressure change and off-fault damage, Bull. Seismol. Soc. Am., Vol. 104, No.2, doi: 10.1785/0120130112

Oglesby, D. (2008), Rupture termination and jump on parallel offset faults, Bull.Seismol. Soc. Am., 98(1), 440-447, doi: 10.1785/0120070163

Oglesby, D. D., S.M. Day, Y.G. Li, and J.E. Vidale (2003), The 1999 Hector Mine earthquake: the dynamics of a branched fault system, Bull. Seismol. Soc. Am., v.93 p. 2459-2476

Ohnaka, M. (1996), Non-uniformity of the constitutive law parameters for shear ruptures and quasi-static nucleation to dynamic rupture: a physical model of earthquake generation process. Proc. Natl. Acad. Sci. USA 93, 3795-3802

Palmer, A. C., and J. R. Rice (1973), Growth of slip surfaces in progressive failure of over-consolidated caly, Proc. R. Soc. London, Ser. A., 332, 527-548Reasenberg, P., and W.L.Ellsworth, Aftershocks of the Coyote Lake earthquake of August 6, 1979: A detailed study, J. Geophys. Res., 87, 10,637-10,655, 1982

Ponti, D. (1993), Quaternary chronostratigraphy and deformation history, Los Angeles Basin, California in National Earthquake Hazards Reduction Program, Summaries of Technical Reports Volume *XXXIV*, U.S. Geol. Surv. Open-File Rept. 93-195, 591

Rice, J.R., and M.P.Cleary (1976), Some basic stress diffusion solutions for fluid-saturated elastic porous media with compressible constituents, Rev. Geophys., 14, 227-241

Rodgers, D.A. (1980), Analysis of pull-apart basin development produced by en echelon strike-slip faults, in Sedimentation in Oblique-Slip Mobile Zones, edited by P.F.Ballance, and H.G. Reading, Spec. Publ. Int. Assoc. Sedimental., 4, 27-41

Ruina, A. (1983), Slip instability and state variable friction law. J. Geophys. Res. 88, 10359-10370

Ruina, A. L., (1980), Friction laws and instability: A quasistatic analysis of some dry friction behavior. Ph.D. Thesis, Brown University, Providence, R. I.

Schwartz, D.P., and K.J.Coppersmith (1984), Fault behavior and characteristic earthquakes: Examples from the Wasatch and San Andreas fault zones, J. Geophys. Res., 89 (B7), 5681-5698, doi: 10.1029/JB089iB07p05681

Scholz, C. H. (2002), The mechanics of Earthquake and Faulting, Cambridge Univ. Press, Cambridge, U. K.

Segall.P., and D.D.Pollard (1980), Mechanics of discontinuous faults, J. Geophys. Res., 85, 4337-4350

Sibson, R.H. (1985), Stopping of earthquake ruptures at dilational fault jogs, Nature, 316(6025), 248-251, doi:10.1038/316248a0

Sibson, R.H., (1986), Rupture interactions with fault jogs, in Earthquake Source Mechanics, Geophys. Monogr. Ser., vol.37, edited by S. Das, J. Boatwright, and C.H.Scholz, AGU, pp. 157-167, Washington, D.C.

Spudich, P., and L. N. Frazer (1984). Use of ray theory to calculate high-frequency radiation from earthquake sources having spatially variable rupture velocity and stress drop, Bull. Seismol. Soc. Am. 74, 2061-2082

Templeton, E. L., and J. R. Rice (2008), Off-fault plasticity and earthquake rupture dynamics: 1. Dry materials or neglect of fluid pressure changes, J. Geophys. Res., 113, B09306, doi: 10.1029/2007JB005529

Viesca, R. C., E. L. Templeton, and J. R. Rice (2008), Off-fault plasticity and earthquake rupture dynamics: 2. Effects of fluid saturation, J. Geophys. Res., 113, B09307, doi: 10.1029/2007JB005530

Wesnousky, S. (1988), Seismological and structural evolution of strike-slip faults. Nature 335, 340-343

Wesnousky S.G. (2006), Predicting the endpoints of the earthquake ruptures, Nature, 444, 358-360

Xu S. and Ben-Zion Y. (2013), Numerical and theoretical analyses of in-plane dynamic rupture on a frictional interface and off-fault yielding patterns at different scales, Geophy. J. Int., 193, 304-320

Xu, X., Yu, G., et. al, (2009), Parameters of coseismic reverse- and oblique-slip ruptures of the 2008 Wenchuan Earthquake, Eastern Tibetan Plateau, Acta Geological Sinica, v.82, p. 673-684